Publisher's PDF, also known as Version of record

Link to published version (if available):
10.1093/mnras/stw1734

Link to publication record in Explore Bristol Research
PDF-document

University of Bristol - Explore Bristol Research
General rights

Deep observations of the Super-CLASS supercluster at 325 MHz with the GMRT: the low-frequency source catalogue

C. J. Riseley,[1,2]★ A. M. M. Scaife,[1] C. A. Hales,[3]† I. Harrison,[1] M. Birkinshaw,[4,5] R. A. Battye,[1] R. J. Beswick,[1] M. L. Brown,[1] C. M. Casey,[6] S. C. Chapman,[7] C. Demetroullas,[1] C.-L. Hung,[6] N. J. Jackson,[1] T. Muxlow[1] and B. Watson[1]

[1]*Jodrell Bank Centre for Astrophysics, Alan Turing Building, School of Physics and Astronomy, The University of Manchester, Oxford Road, Manchester M13 9PL, UK*
[2]*School of Physics and Astronomy, University of Southampton, Highfield, Southampton SO17 1BJ, UK*
[3]*National Radio Astronomy Observatory, PO Box 0, Socorro, NM 87801, USA*
[4]*H. H. Wills Physics Laboratory, University of Bristol, Tyndall Avenue, Bristol BS8 1TL, UK*
[5]*Harvard–Smithsonian Center for Astrophysics, 60 Garden St, Cambridge, MA 02138, USA*
[6]*Department of Astronomy, The University of Texas at Austin, 2515 Speedway Blvd Stop C1400, Austin, TX 78712, USA*
[7]*Department of Physics and Atmospheric Science, Dalhousie University, Coburg Road, Halifax B3H 1A6, Canada*

ABSTRACT

We present the results of 325 MHz Giant Metrewave Radio Telescope observations of a supercluster field, known to contain five Abell clusters at redshift $z \sim 0.2$. We achieve a nominal sensitivity of $34\,\mu\text{Jy beam}^{-1}$ towards the phase centre. We compile a catalogue of 3257 sources with flux densities in the range $183\,\mu\text{Jy} - 1.5\,\text{Jy}$ within the entire $\sim 6.5\,\text{deg}^2$ field of view. Subsequently, we use available survey data at other frequencies to derive the spectral index distribution for a sub-sample of these sources, recovering two distinct populations – a dominant population which exhibit spectral index trends typical of steep-spectrum synchrotron emission, and a smaller population of sources with typically flat or rising spectra. We identify a number of sources with ultrasteep spectra or rising spectra for further analysis, finding two candidate high-redshift radio galaxies and three gigahertz-peaked-spectrum radio sources. Finally, we derive the Euclidean-normalized differential source counts using the catalogue compiled in this work, for sources with flux densities in excess of $223\,\mu\text{Jy}$. Our differential source counts are consistent with both previous observations at this frequency and models of the low-frequency source population. These represent the deepest source counts yet derived at 325 MHz. Our source counts exhibit the well-known flattening at mJy flux densities, consistent with an emerging population of star-forming galaxies; we also find marginal evidence of a downturn at flux densities below $308\,\mu\text{Jy}$, a feature so far only seen at 1.4 GHz.

Key words: surveys – radio continuum: general.

1 INTRODUCTION

Deep radio surveys of the extragalactic source population are powerful tools with which to probe a wide range of source populations across a variety of environments and redshifts. In previous decades, optical surveys have been preferred for the study of the formation, interactions and evolution of galaxies. However, radio emission is important for galaxy population studies, as the synchrotron emission is a clear indicator of magnetic fields from star formation and active galactic nuclei (AGN). Additionally, the radio emission is essentially unaffected by dust obscuration and as such provides a powerful tracer of the evolution of star-forming galaxies (SFG) and AGN with redshift.

All-sky surveys – for example the Very Large Array (VLA) Faint Images of the Radio Sky at Twenty-Centimetres (FIRST; Becker, White & Helfand 1994) survey and the NRAO VLA Sky Survey (NVSS; Condon et al. 1998) at 1.4 GHz, and the 325 MHz Westerbork Northern Sky Survey (WENSS; Rengelink et al. 1997) – have been effective in identifying large numbers of bright radio sources and have led to studies of the populations they represent. At higher frequencies ($\nu \gtrsim 1.4$ GHz) and/or higher flux densities ($S \gtrsim 1$–10 mJy at 1.4 GHz), the dominant population of sources are

---

★ E-mail: c.j.riseley@manchester.ac.uk
† Jansky Fellow of the National Radio Astronomy Observatory.

radio-loud AGN (for example, Condon 1984; Becker et al. 1994; Condon et al. 1998; Gruppioni et al. 1999; Afonso et al. 2005; Bondi et al. 2008).

Moving to fainter flux densities, the contribution from SFG and radio-quiet (RQ) AGN become increasingly important, and these sources are believed to dominate at $S \lesssim 0.1$ mJy (for example, Richards et al. 1999; Muxlow et al. 2005; Padovani et al. 2007, 2009, 2015; Mainieri et al. 2008; Ibar et al. 2009; Bonzini et al. 2013). The physics of low-luminosity SFG is still poorly understood; all-sky surveys are too shallow to recover sufficient numbers of these faint sources to infer much detail. Increasingly deep surveys such as the VLA-COSMOS survey (for example, Schinnerer et al. 2004) as well as smaller, deep fields (e.g. Morganti et al. 2004; Miller et al. 2013) have recovered sources down to $\sim \mu$Jy flux densities at 1.4 GHz. Radio emission from SFG is comprised of two components: synchrotron emission dominates at low frequencies, whereas thermal bremsstrahlung (free–free emission) from the ionized interstellar medium dominates at higher frequencies (for example, Condon 1992; Bressan, Silva & Granato 2002; Clemens et al. 2008). Whilst synchrotron emission presents itself with typical spectral index[1] of $\alpha \simeq -0.8$, free–free emission has a flatter spectrum (typically $\alpha \simeq -0.1$). In addition to these features at high frequency, SFG spectra exhibit a number of other features below 1 GHz, with bends and inversions detected in some spectra (Clemens et al. 2010).

Surveys at low frequencies (for example, Wieringa 1991; Garn et al. 2008a,b; Owen et al. 2009; Sirothia et al. 2009; Sirothia, Saikia & Burgarella 2010; Mauch et al. 2013; Smolčić et al. 2014) open a new window for study, offering a number of advantages over their higher frequency counterparts. Low-frequency observations are powerful at detecting (ultra-)steep spectrum sources, which are often galaxies at high redshift (Miley & De Breuck 2008 and references therein). Low-frequency observations also enable detailed studies of the radio synchrotron spectral index, which allows for more precise characterization of the source properties.

In this work, we present the results of a deep 325 MHz continuum survey of a supercluster field, performed using the Giant Metrewave Radio Telescope (GMRT) and carried out as part of the Super-Cluster Assisted Shear Survey (Super-CLASS). The remainder of this paper is divided as follows: we first introduce the Super-CLASS project in Section 1.1; subsequently we detail the observations and data reduction methodology in Section 2. We present our results in Section 3, including a sample from our source catalogue; we verify the catalogue and analyse the statistical properties in Section 4. In Section 5 we derive the spectral index distribution and identify sources with steep and/or inverted spectra for further study, which may constitute ultrasteep spectrum (USS) radio sources or gigahertz-peaked spectrum (GPS) radio sources. We derive the source counts distribution from our catalogue, as well as evaluate the various bias and incompleteness corrections that must be applied, in Section 6. Finally, we draw our conclusions in Section 7. All errors are quoted to 1σ. We adopt the spectral index convention that $S \propto \nu^{\alpha}$ where the radio spectral index $\alpha < 0$. We assume a concordance cosmology of $H_0 = 73 \mathrm{km \, s^{-1} \, Mpc^{-1}}$, $\Omega_m = 0.27$, $\Omega_\Lambda = 0.73$. At a redshift of $z = 0.2$, representative of the constituent clusters of the Super-CLASS supercluster, an angular size of 1 arcsec corresponds to a physical size of 3.2 kpc.

Table 1. Properties of galaxy clusters constituting the Super-CLASS supercluster.

Name	RA (J2000)	Dec (J2000)	z	L_x (0.1–2.4 keV) ($\times 10^{44}$ erg s^{-1})
Abell 968	$10^h21^m09\overset{s}{.}5$	$+68°15'53''$	0.195	0.401
Abell 981	$10^h24^m24\overset{s}{.}8$	$+68°06'47''$	0.202	1.670
Abell 998	$10^h26^m17\overset{s}{.}0$	$+67°57'44''$	0.203	0.411
Abell 1005	$10^h27^m29\overset{s}{.}1$	$+68°13'42''$	0.200	0.268
Abell 1006	$10^h27^m37\overset{s}{.}2$	$+67°02'41''$	0.204	1.320

Notes. References: Redshift, z: Huchra et al. (1990), X-ray luminosity, L_x: BAX data base; Sadat et al. (2004).

1.1 The Super-CLASS

Weak lensing in the radio regime is emerging as promising cosmological probe, as many of the issues which strongly affect optical lensing studies (such as atmospheric effects and anisotropic PSFs) are negated by shifting to radio wavelengths. While measurements of cosmic shear on scales of 1–4 degrees have been made at radio wavelengths (for example, Chang, Refregier & Helfand 2004, and see also Patel et al. 2010) previous shear surveys have been severely limited by resolution, field of view, and low source counts. A large, high-resolution catalogue is required to disentangle the shear signal (a factor of ~ 0.01) from intrinsic source ellipticity (typically ~ 0.3). Recent work by Demetroullas & Brown (2016) has demonstrated that biases in shear measurements can be mitigated by cross-correlating both radio and optical survey data

Of the current generation of instruments, perhaps the best suited to studies of cosmic shear is the expanded Multi-Element Remote-Linked Interferometer Network (e-MERLIN). A number of legacy surveys are currently underway with e-MERLIN, including the Super-CLASS project.[2]

Super-CLASS is a wide-area, deep e-MERLIN legacy survey at L band (reference frequency 1.4 GHz) targeting a region of sky known to contain five moderate-redshift ($z \sim 0.2$) Abell clusters – A968, A981, A998, A1005 and A1006 (Abell, Corwin & Olowin 1989). Some observational properties of these clusters are listed in Table 1. Hereafter this region is referred to as the Super-CLASS field. The principal goal of the project is to detect the effects of cosmic shear in a supercluster environment, where the increased level of structure should allow for a statistically significant detection of shear over a wide range of scales. However, a number of ancillary science goals exist, such as investigation of polarization properties of AGN and SFG, studies of cosmic magnetism in cluster- and supercluster environments, classifying the galaxy population in the supercluster, and detailed studies of the radio source population at μJy flux densities.

A wide range of other instruments are involved, including the Karl G. Jansky Very Large Array (JVLA) and LOw-Frequency Array (LOFAR; van Haarlem et al. 2013) in the radio band, and a number of optical and mm/sub-mm wavelength telescopes. The weak lensing component of the survey is similar in manner (although with lower source densities and on a smaller field) to those that may ultimately be conducted by the Square Kilometre Array (SKA; http://skatelescope.org). For more details on weak lensing with the SKA see for example, Brown et al. (2015). See Harrison

---

[1] Adopting the convention $S \propto \nu^{\alpha}$.

[2] For more details, see http://www.e-merlin.ac.uk/legacy/projects/superclass.html

Table 2. Summary of GMRT pointings on the Super-CLASS field. For each pointing, we list the integration time (τ_{int}) as well as the percentage of data that was used (i.e. unflagged) in the final image, as well as the predicted thermal noise.

RA (J2000)	Dec (J2000)	τ_{int} (s)	Unflagged (per cent)	$\sigma_{rms}(\mu Jy\ beam^{-1})$ Thermal	Measured
$10^h21^m56\overset{s}{.}13$	$68°09'44''\!.8$	14.8×10^3	66.0	33.9	46.4
$10^h24^m17\overset{s}{.}12$	$67°35'26''\!.7$	15.3×10^3	62.9	34.2	42.9
$10^h26^m31\overset{s}{.}43$	$67°01'01''\!.4$	15.0×10^3	63.8	34.3	42.8
$10^h28^m50\overset{s}{.}28$	$67°35'25''\!.0$	14.5×10^3	64.7	34.6	44.0
$10^h26^m32\overset{s}{.}15$	$68°09'57''\!.5$	14.5×10^3	68.0	33.8	41.5
$10^h24^m15\overset{s}{.}01$	$68°44'23''\!.0$	14.6×10^3	66.8	34.0	44.8

Table 3. Summary of the GMRT observations of the Super-CLASS field.

Date	Start time (IST)	Hours observed	# Antennas	Antennas missing throughout run	Comments
2014 Jan 09	23:00	10.3	29	S02	W02 stopped at 01:36. MESB power failures at 23:26 for 6 min and at 01:33 for 20 min.
2014 Jan 11	02:30	7.5	27	W02, C04, S02	C09 out 05:12–05:44. GSB problem at 07:44 forced reset.
2014 Jan 12	04:45	5.3	30	–	W02 (C10) stopped at 08:47 (09:25).
2014 Jan 13	05:00	4.3	30	–	–
2014 Jan 14	21:00	12.5	30	–	W02 (C10) stopped at 08:47 (09:10).

et al. (2016) for cosmology forecasts from weak lensing with the SKA; for simulated catalogues see Bonaldi et al. (2016).

2 OBSERVATIONS AND DATA REDUCTION

2.1 Observing details

The Super-CLASS field was observed in 2014 January using the GMRT over the course of five nights, under project code 25_052 (P.I. Scaife, A.). At 325 MHz, the GMRT has a large primary beam full width at half-maximum (FWHM) of 84 arcmin. To achieve as close to uniform coverage as possible across the e-MERLIN survey area while retaining efficiency, the Super-CLASS field was covered in six close-packed pointings, summarized in Table 2.

The GMRT was used with the GMRT Software Backend (GSB; Roy et al. 2010) in default configuration in total intensity mode, with an acquisition bandwidth of 33 MHz, 256 channels, and an integration time of 8.05 s. Calibrator sources 3C 286 and 3C 48 were scanned for 10–15 min at the beginning and end of each observing run. 3C 286 was typically available for both initial and final calibrator scans; 3C 48 was only observed on two nights when 3C 286 was unavailable for one or other of the calibrator scans.

Throughout the observing runs, a minimum of 26 of the 30 antennas were functional at all times; those missing may have been offline for a number of reasons including being taken for painting, problems with the hardware, or experiencing particularly strong radio frequency interference (RFI). On one night (January 9) power failures forced a temporary halt in data collection, and on one night (January 11) issues with the GSB forced a restart. Data taken during these periods were inspected for quality, and compromised data were discarded. In Table 3, we present a summary of the observa-

tions, including integration time, number of antennas, any missing antennas, and any general comments on each night's observing.

Scans were conducted in a 23 min//4 min (target//calibrator) ratio; to maximize *uv*-coverage for each pointing, scans on the same field were repeated only after a full cycle through all fields. The interleaved calibrator was observed after each pointing. The total integration time per pointing was of the order of 14.8×10^3 s, for a total integration time on target of 24.6 h. The theoretical noise was derived using the following expression:

$$\sigma_{th} = \frac{\sqrt{2}T_{sys}}{G\sqrt{n(n-1)f_d\Delta\nu\tau_{int}}}, \qquad (1)$$

where the system temperature $T_{sys} = 106$ K, the antenna gain $G = 0.32$ K Jy^{-1} antenna^{-1}, n is the number of working antennas (taken as being 26, the minimum number functioning at any given time). $\Delta\nu$ is the bandwidth available; after removal of edge channels where the sensitivity drops off rapidly, $\Delta\nu$ reduces from 33 to 30 MHz. τ_{int} is the integration time on target, and f_d is the fraction of data used (i.e. the unflagged fraction). In Table 2, we also list the integration time, the fraction of the data that was used and the expected noise for each pointing. The measured noise per pointing is also listed in Table 2, from which it is clear that we achieve a sensitivity of approximately $1.3 \times \sigma_{th}$. The final *uv*-coverage of a single pointing is shown in Fig. 1; it is clear that the *uv*-plane is well filled out to approximately $10-15$ kλ.

2.2 Data reduction

2.2.1 Calibration

The data were reduced using the Source Peeling and Atmospheric Modelling (SPAM) software (Intema et al. 2009) which
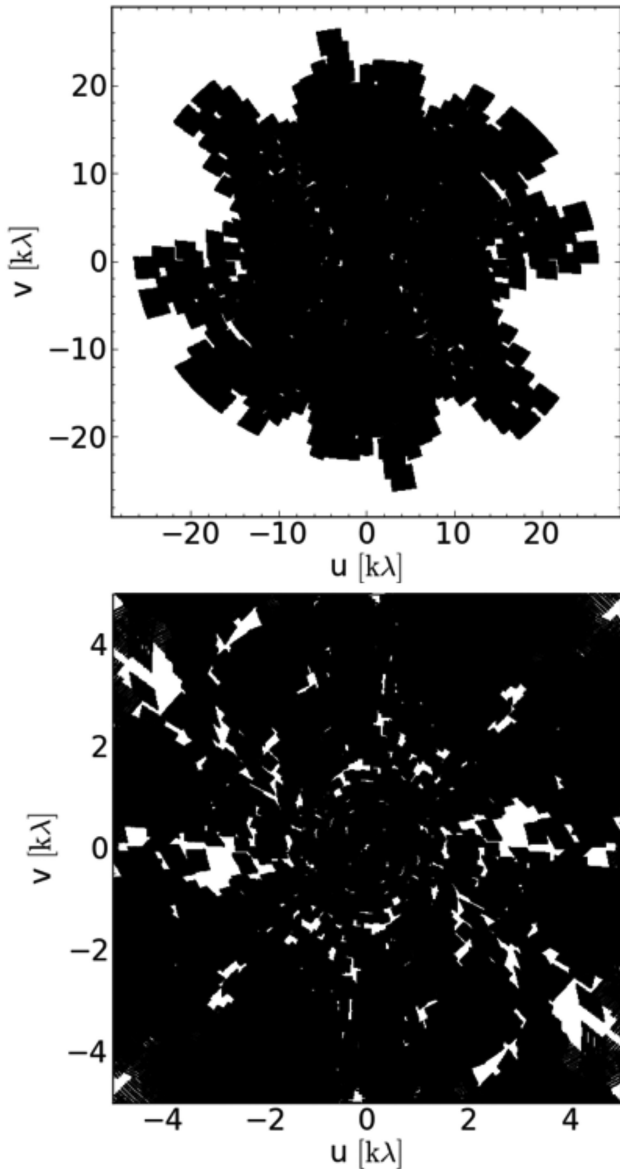
Figure 1. Typical *uv*-coverage of a single pointing on the Super-CLASS field. Top panel: plot showing coverage of the full *uv*-plane. Bottom panel: zoom on the central portion of the *uv*-plane, illustrating the coverage on short baselines.

employs NRAO Astronomical Image Processing Software (AIPS) tasks through the ParselTongue interface (Kettenis et al. 2006). SPAM employs the Scaife & Heald (2012) flux density scale, which yields a flux density of 24.138 Jy and spectral index $\alpha = -0.197$ for 3C 286 at 325 MHz; for 3C 48 the flux density and spectral index are 43.742 Jy and $\alpha = -0.607$, respectively. Intema et al. (2009) describe data reduction with SPAM in detail; however, here we will summarize the process.

Following removal of edge channels, the data were averaged by a factor of 4 in frequency (yielding 64 channels of width 502.8 kHz) and 2 in time, as a compromise between improving data processing speed and mitigating bandwidth-/time-smearing effects. Prior to calibration, the data were visually inspected for strong RFI and bad antennas/baselines. Calibration solutions were derived for 3C 286 and 3C 48 using standard techniques in SPAM and applied to the

target field. The interleaved calibrators are not used during the reduction process.[3] Instead, SPAM performs an initial phase calibration and astrometry correction using a sky model derived from the NVSS (Condon et al. 1998) before proceeding with three rounds of direction-independent phase-only self-calibration.

Following the self-calibration, SPAM identifies strong sources within the primary beam FWHM that are suitable for direction-dependent calibration and ionospheric correction. Only sources with well-defined astrometry are selected, yielding a catalogue of approximately 20 sources. Subsequently, SPAM performs direction-dependent calibration on a per-facet basis, using the solutions to fit a global ionospheric model, as described by Intema et al. (2009). Throughout the reduction process, multiple automated flagging routines are used between cycles of imaging and self-calibration in order to reduce residual RFI and clip outliers. Across the six fields, around 32–37 per cent of the data were flagged out; this is not uncommon for GMRT data at this frequency – for example, approximately 60 per cent of the data were flagged in the work of Sirothia et al. (2009). Additionally, the average flagged fraction was 40 per cent in Mauch et al. (2013). Flagging statistics for each pointing are also listed in Table 2.

2.2.2 Imaging

During the self-calibration and imaging cycles, images were made using an AIPS ROBUST of -1.0 in order to achieve a compromise between sensitivity and resolution.[4] All imaging was performed with facet-based wide-field imaging as implemented in SPAM.

The direction-dependent and ionospheric calibration routine described above was repeated on each field separately. Following this calibration routine, the final images of all six fields were convolved to a common circular synthesized beam of FWHM 13 arcsec. These final images were then corrected for primary beam attenuation (with a cutoff of 30 per cent) and mosaicked in the image plane, weighted by the inverse of the local rms, using AIPS tasks as employed by SPAM.

3 RESULTS

Fig. 2 shows the sensitivity of the final mosaicked image, derived using the PYTHON Blob Detection and Source Measurement (PYBDSM;[5] Mohan & Rafferty 2015) software. From Fig. 2, the typical noise in the image is low, apart from a number of regions near bright and/or complex sources: the image rms is below $50\,\mu$Jy beam^{-1} for the inner portion of the mosaic, and below $100\,\mu$Jy beam^{-1} for the majority of the mosaic. We present a cutout region of the GMRT survey area in Fig. 3 as an example of the image quality recovered from this work. The GMRT image has a nominal off-source noise of $\sigma_{nom} = 34\,\mu$Jy beam^{-1} in this region; from Fig. 3, it appears that the quality is generally very high, although artefacts caused by residual phase and/or amplitude errors remain around some of the most complex sources, and there are some dynamic

---

[3] The interleaved calibrators (0949+662 and 1101+724) were used to track atmospheric effects and data quality during the observing run itself.

[4] An AIPS ROBUST $= -5.0$ indicates pure uniform weighting, for maximum resolution; ROBUST $= +5.0$ indicates pure natural weighting, for maximum sensitivity.

[5] PYBDSM: http://www.astron.nl/citt/pybdsm/
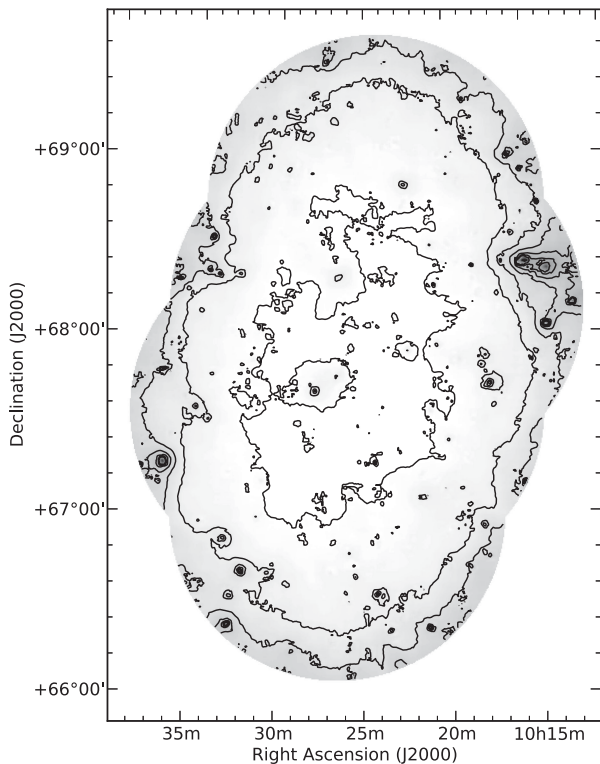
Figure 2. Grey-scale image showing the local rms noise of the final mosaicked GMRT image, derived using PYBDSM (see Section 3.1). The colour scale ranges from 50–750 μJy beam^{-1}; contours are [1, 2, 3, 4, 5, 6, 7] × 50 μJy beam^{-1}.

range issues associated with some of the brighter sources in the field.

3.1 Source catalogue

A catalogue of sources was compiled with PYBDSM. We compiled a catalogue of sources above $5\sigma_{local}$ in significance, where σ_{local} is the local noise level. PYBDSM derives a sensitivity map from the data and determines the local noise iteratively in a moving box. Subsequent 'islands' are isolated above a user-defined threshold (set to $4\sigma_{local}$) and Gaussians fitted to regions above a user-defined peak (set to $5\sigma_{local}$). In order to reduce the number of spurious sources fitted to deconvolution artefacts, we defined two moving boxes: a 'large' box of 200 pixels was used across the entire image, and a 'small' box of 50 pixels was used in regions close to sources of high signal to noise. To better model the extended emission in the field, we also used the wavelet functionality of PYBDSM to decompose the residual image into wavelet images on a small number of scales, fitting to islands initially identified by PYBDSM during the Gaussian fitting routine.

The catalogue produced by PYBDSM was visually inspected; we removed any false detections arising from artefacts near complex/bright sources, and any sources that were cut by the primary beam cutoff (a total of 10 sources were removed). The final number of sources in our catalogue is 3257, and we present a sample from the full catalogue in Table 4. The full catalogue is available online through CDS (http://cds.u-strasbg.fr). Hereafter we refer to our catalogue as the 325 MHz Super-CLASS-GMRT (SCG325) catalogue. A short description of the catalogue is as follows.

Column (0): Source name, following the nomenclature SCG325_Jh:m:s+°:′:″.

Columns (1) and (2): Source right ascension (RA) and declination (DEC) in J2000 coordinates in sexagesimal format.

Column (3): fitted peak flux density at 325 MHz in mJy beam^{-1}, with its associated uncertainty. The measurement uncertainty is taken as the fitted error plus five per cent of the peak flux density, added in quadrature.

Column (4): fitted integrated flux density at 325 MHz in mJy, with its associated uncertainty. The measurement uncertainty is taken as sum of the fitted error plus five per cent of the integrated flux density, again added in quadrature.

Columns (5), (6) and (7): deconvolved major and minor axes FWHM (in arcsec) and position angle (PA) of the elliptical Gaussian (in degrees east of north). Sizes are only quoted for resolved sources; if unresolved, these columns are marked with a dash (−). See Section 4.1.5 for our definition of resolved and unresolved sources.

Columns (8), (9) and (10): error in the deconvolved major and minor axes FWHM (in arcsec) and position angle (PA) of the elliptical Gaussian (in degrees east of north). These are quoted only for sources that are resolved; if unresolved these columns are marked with a dash (−).

3.2 Completeness

To quantify the efficiency with which PYBDSM detects sources in our field, we established a number of Monte Carlo simulations for sources with flux densities at log-spaced intervals between 160 μJy and 1.5 Jy. For each flux density, 10 catalogues of 160 point sources were generated, with positions randomized for each catalogue. These were then inserted into the residual map generated by PYBDSM, and catalogued in the same manner as the real data. Subsequently, the recovered sources were cross-referenced with the known simulated population to establish the fraction of sources missed as a function of flux density.

This missed fraction as a function of flux density is presented in Fig. 4, with the fitted exponential function shown as a dashed curve. The fit suggests our catalogue is 95 per cent complete at a flux density $S = 1.25$ mJy, and the completeness drops rapidly below 1 mJy.

4 ANALYSIS

4.1 Verification

The Super-CLASS region studied in this work has been covered by a number of surveys in the radio band. Catalogues exist at 74 MHz from the VLA Low-frequency Sky Survey (VLSS; Cohen et al. 2007) and VLSS-Redux (VLSSR; Lane et al. 2014), at 325 MHz from the WENSS (Rengelink et al. 1997) and at 1.4 GHz from the NVSS (Condon et al. 1998). The high declination of the field puts this region outside the coverage of the VLA-FIRST survey (Becker et al. 1994). In this section, we use the available survey data to validate our GMRT source catalogue.

It is important to note that in all our comparisons, the flux density measurements from the literature have been adjusted to bring them in line with the Scaife & Heald (2012) flux scale adopted in this work (hereafter SH12). The flux density scale of WENSS is complex, having been set using observations of the sources 3C 48, 3C 147, 3C 286 and 3C 295. The correction factor to scale the WENSS survey to the SH12 flux scale is an average correction
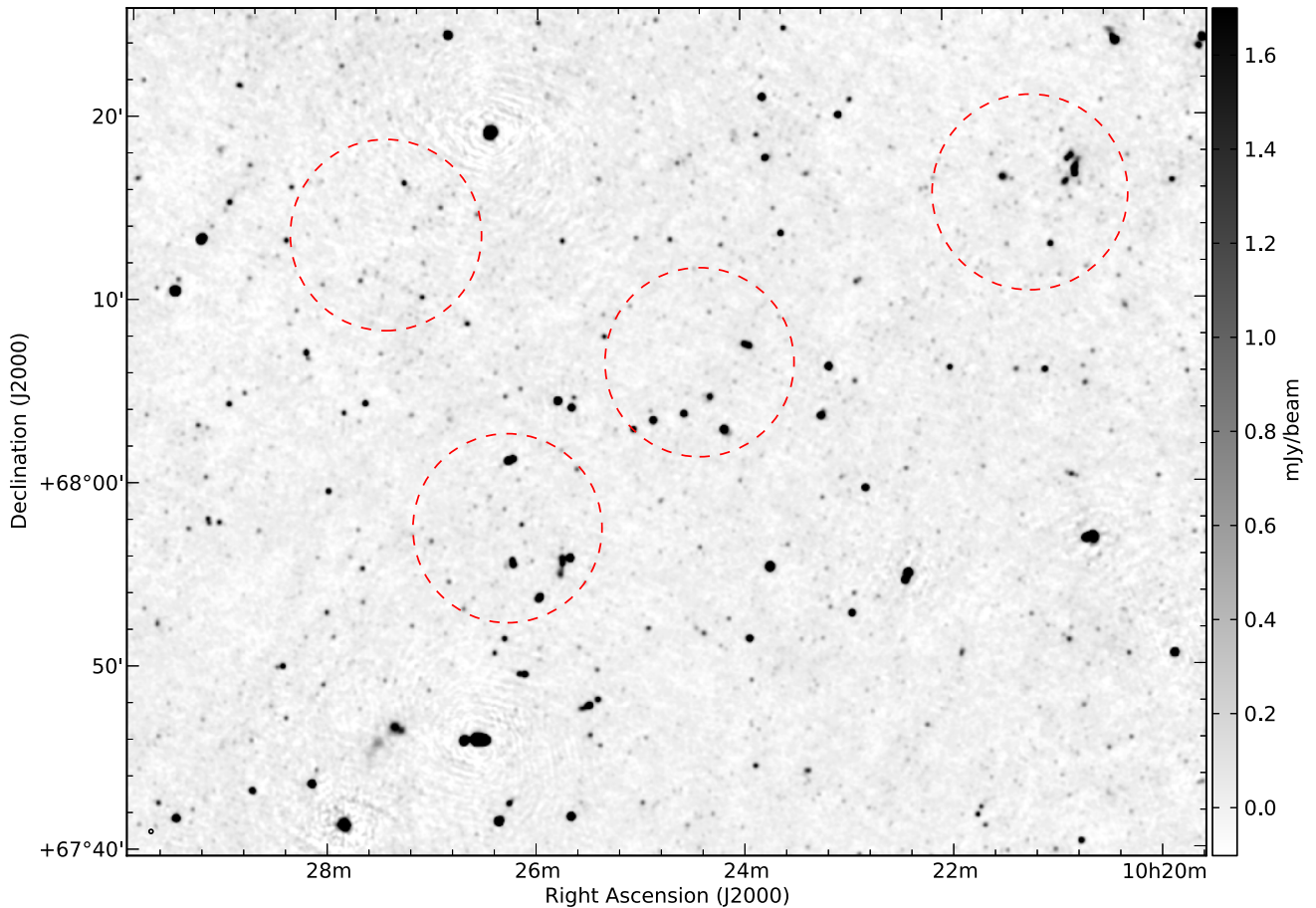
Figure 3. Example region from the Super-CLASS field as observed with the GMRT. The grey-scale ranges from $-3\sigma_{nom}$ to $50\sigma_{nom}$, where the nominal noise level is $\sigma_{nom} = 34$ μJy beam^{-1}. The restoring beam FWHM is 13 arcsec. The mosaicked image is corrected for the primary beam response of the GMRT. We note that while the noise in this region is generally low, and varies smoothly, some residual errors remain around some bright and/or complex sources. Dashed red circles trace a radius of 1 Mpc, centred on the reference coordinates of the clusters A968, A981, A998 and A1005 (see Table 1).

Table 4. Excerpt from the 325 MHz SCG325 catalogue. The full catalogue is available through CDS (http://cds.u-strasbg.fr). Column (0): Source name, following the nomenclature SCG325_Jh:m:s+°:′:″. Columns (1) and (2): right ascension and declination in sexagesimal format, J2000 reference. Column (3): peam flux density at 325 MHz and associated error. Column (4): integrated flux density at 325 MHz and associated error. For unresolved sources, this is taken as being equal to the peak flux density, see Section 4.1.5. Columns (5), (6) and (7): deconvolved source major axis, minor axis and position angle. Columns (8), (9) and (10): uncertainty in the deconvolved major axis, minor axis and position angle. Columns (5) to (10) list a dash (–) if the source is unresolved.

(0) Source name	(1) RA (J2000) h:m:s	(2) DEC (J2000) °:′:″	(3) S_{peak} (mJy beam^{-1})	(4) S_{int} (mJy)	(5) $\theta_{maj.}$ (arcsec)	(6) $\theta_{min.}$ (arcsec)	(7) PA (deg)	(8) $\Delta(\theta_{maj.})$ (arcsec)	(9) $\Delta(\theta_{min.})$ (arcsec)	(10) Δ(PA) (deg)
SCG325_J103820+672701	10 38 20.09	67 27 01.2	2.52 ± 0.22	3.43 ± 0.32	9.13	6.42	58.45	1.15	0.97	35.37
SCG325_J103820+673505	10 38 20.80	67 35 05.8	0.89 ± 0.18	1.08 ± 0.29	–	–	–	–	–	–
SCG325_J103809+672129	10 38 09.58	67 21 29.8	1.42 ± 0.22	1.91 ± 0.34	11.59	1.31	73.44	2.77	1.63	25.97
SCG325_J103809+672449	10 38 09.32	67 24 49.4	1.44 ± 0.20	1.35 ± 0.32	–	–	–	–	–	–
SCG325_J103805+672256	10 38 05.68	67 22 56.6	4.68 ± 0.38	6.45 ± 0.55	10.84	4.46	70.49	0.77	0.52	11.91
SCG325_J103807+673552	10 38 07.42	67 35 52.3	0.91 ± 0.18	1.07 ± 0.29	–	–	–	–	–	–
SCG325_J103804+674543	10 38 04.88	67 45 43.7	11.38 ± 0.83	20.77 ± 1.55	–	–	–	–	–	–
SCG325_J103747+671514	10 37 47.72	67 15 14.1	5.05 ± 0.46	7.88 ± 0.71	13.34	5.59	92.72	1.20	0.73	12.77
SCG325_J103746+671551	10 37 46.58	67 15 51.5	1.79 ± 0.26	2.25 ± 0.42	–	–	–	–	–	–
SCG325_J103749+672539	10 37 49.18	67 25 39.5	1.68 ± 0.19	1.93 ± 0.30	–	–	–	–	–	–

across the discrete set of WENSS calibrators. It would be incorrect to apply this factor to any localized area of the sky as the difference between the flux densities of the WENSS calibrators and the SH12 source models range from ∼1 to ∼18 per cent (see Rengelink et al. 1997, SH12). We note that, given the small difference between the native WENSS flux densities in this region

and the GMRT values measured here (see Section 4.1.3) as well as the RA range, this field was likely calibrated using either 3C 147 or 3C 48. These calibrators both have ratios to the SH12 scale within the measurement uncertainty. Hence, we do not apply a correction factor to the flux densities from WENSS during catalogue verification.
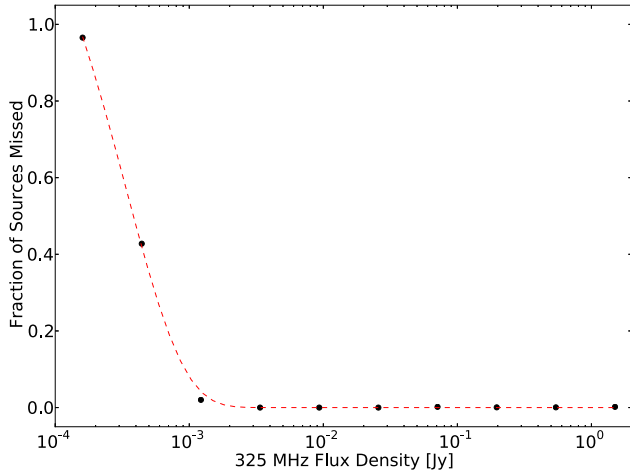
Figure 4. Fraction of sources missed as a function of 325 MHz flux density. Black points mark flux densities where simulated catalogues were analysed, dashed line marks the exponential fit.

The SH12 flux scale is calibrated on the RCB flux density scale (Roger, Costain & Bridle 1973); at frequencies greater than 300 MHz, the RCB flux density scale is consistent with the KPW flux density scale (Kellermann, Pauliny-Toth & Williams 1969). Therefore we can use table 7 from Baars et al. (1977) to adjust the flux density of sources on the Baars scale before comparing them with these GMRT data; hence the NVSS flux densities have been adjusted by a factor of 0.972. The VLSS and VLSSR were also calibrated on the Baars flux density scale; measurements from the VLSS and VLSSR catalogues have been adjusted by a mean factor of 1.10 to align with the SH12 scale, see Lane et al. (2014).

4.1.1 Match criteria

We attempted to match all sources in our catalogue to their equivalent in other catalogues. We matched sources from the SCG325 catalogue to reference catalogues (NVSS/WENSS) using a maximum offset of twice the synthesized beam FWHM of the GMRT image (i.e. 26 arcsec). Given the difference in resolution between the SCG325 catalogue and the references – 13 arcsec for the SCG325 catalogue compared to 45 arcsec (54 arcsec cosecδ) arcsec for NVSS (WENSS) – we would expect a number of previously unresolved sources to become resolved in the GMRT data. Where this was the case, flux densities of the SCG325 sources were summed for the purposes of flux density verification and spectral index derivation.

The SCG325 catalogue consists of a total of 3257 sources. We find 335 sources in the NVSS catalogue (Condon et al. 2002) with matches in our catalogue, and 137 sources in the WENSS catalogue (de Bruyn et al. 2000) with SCG325 counterparts. From visual inspection, we note a total of 13 sources present in the NVSS catalogue that do not have counterparts in the SCG325 catalogue; all have integrated flux densities in the range 2.2–3.2 mJy at 1.4 GHz, and peak flux densities below 2.5 mJy beam^{-1} (based on the NVSS mosaic images). In the GMRT image, the peak flux density at these positions ranged from $-80\,\mu$Jy beam^{-1} to 240 μJy beam^{-1}. In two cases, potential matches were nearby but separated by more than three times the GMRT restoring beam FWHM. For the remaining 11, no nearby SCG325 catalogue sources exist, and manual fits to these positions recovered no significant flux density. The positions of these sources and their integrated flux densities from the NVSS are presented in Table 5.

Table 5. Sources in the NVSS catalogue that do not have SCG325 counterparts.

RA (J2000) h:m:s	Dec (J2000) $\circ$:':"	S_{int} (1.4 GHz) (mJy)	Comments
10 16 37.25	67 26 34.7	2.3 ± 0.4	–
10 20 41.93	68 14 40.5	2.6 ± 0.5	–
10 23 54.07	66 36 29.5	2.6 ± 0.5	–
10 24 39.65	68 05 54.2	2.3 ± 0.5	–
10 26 23.13	67 51 21.5	2.8 ± 0.5	a
10 27 32.25	67 45 16.8	2.9 ± 0.5	b
10 29 23.90	68 06 11.3	2.4 ± 0.4	–
10 29 35.18	69 10 04.3	2.3 ± 0.4	–
10 29 51.30	67 38 50.5	2.2 ± 0.4	–
10 29 55.05	68 24 28.0	2.7 ± 0.4	–
10 33 12.42	68 19 24.6	2.2 ± 0.4	–
10 35 12.61	67 35 08.7	3.2 ± 0.5	–
10 37 43.52	67 38 43.6	2.8 ± 0.5	–

^{a}Two SCG325 sources are nearby, but separated by more than three times the GMRT synthesized beam FWHM.
^{b}An extended SCG325 source is nearby, but separated by more than three times the GMRT synthesized beam FWHM.
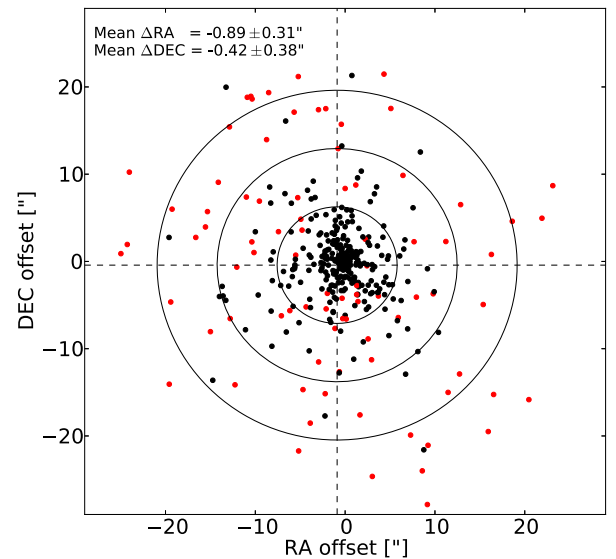

Figure 5. Offset in RA and DEC of the sources in the GMRT field of view that have matches in the NVSS catalogue. The mean ΔRA (ΔDEC) is -0.89 ± 0.31 (-0.42 ± 0.38) arcsec, and is indicated by the dashed lines. Circles correspond to [1, 2, 3]σ_{pos} where the standard deviation in position offset, $\sigma_{pos} = 6.68$ arcsec. Red points mark multiple SCG325 sources which have a single association in the NVSS catalogue.

4.1.2 Astrometry

Sources in the NVSS catalogue are known to have positional accuracies better than around an arcsecond for sources with integrated flux densities greater than 15 mJy, and accuracies better than 7 arcsec for fainter sources (Condon et al. 1998). Using the NVSS catalogue RA and DEC for reference, we determined the position offsets for the 335 sources present in the GMRT data which have matches in the NVSS catalogue. The offsets in RA and DEC are presented in Fig. 5.

From Fig. 5, it is clear that the vast majority of sources in the GMRT catalogue have very little offset with respect to the NVSS catalogue. However, a number of sources lie more than 3σ away
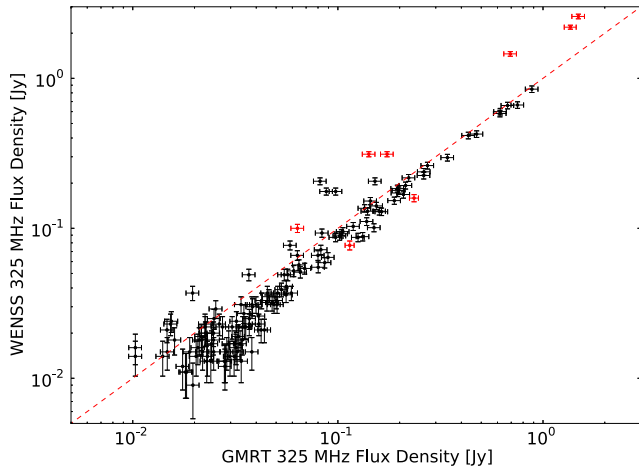
Figure 6. Integrated flux densities of sources common to both the SCG325 catalogue and the WENSS catalogue. The dashed line indicates a flux density ratio equal to unity. The WENSS flux densities have been corrected to bring them in line with the SH12 flux scale adopted in this work. Red points mark sources resolved by WENSS, black points mark unresolved WENSS sources.

from the NVSS reference position. From inspection, these high offsets are caused by one of a number of factors. Foremost, the high offset may be due to single NVSS sources becoming resolved into multiple, separate sources as a result of the superior resolution. This is the case for the vast majority of outliers; we have indicated these cases in Fig. 5. For the remaining sources of high offset, it is typically the case that single NVSS sources become complex or extended at 325 MHz; in these situations the position offset is due to differences in the location of the emission peak.

The mean offsets in right ascension and declination are ΔRA $(\Delta$DEC$) = -0.89 \pm 0.31 \ (-0.42 \pm 0.38)$ arcsec. The synthesized beam FWHM of these GMRT observations is 13 arcsec. Hence, within the uncertainties, the positions of the SCG325 sources are consistent with the NVSS reference positions.

4.1.3 Flux density

The WENSS catalogue contains sources above a 5σ limiting peak flux density of 18 mJy beam^{-1}. Given that the WENSS observations were conducted at approximately the same frequency as this work, we are able to directly compare the integrated flux densities of sources common to both catalogues. Within the mosaicked GMRT area, we find 137 sources in the WENSS catalogue, of which six are resolved by WENSS. In Fig. 6, we present the integrated flux densities for sources common to both the WENSS and SCG325 catalogues. We take the error in the WENSS flux density measurements to be 5 per cent of the integrated flux density plus the nominal image noise, added in quadrature.

From Fig. 6 it appears that the flux densities of sources recovered by the GMRT are generally consistent with their counterparts in WENSS. There is a slight excess at high flux densities, although it is possible that this can be attributed to improved ionospheric calibration. At lower flux densities there is broad scatter in the flux density ratio. Several effects may contribute to this difference – first, the improved calibration routine may allow us to recover more flux from these sources. Secondly, the superior sensitivity and resolution of these GMRT observations may play a role: of the SCG325 sources with point-source counterparts in WENSS,

around half become extended at the resolution of these GMRT data, particularly those sources of lower integrated flux density. The high sensitivity of these GMRT observations may go some way to explaining this scatter, recovering fainter emission from these resolved sources.

We have performed two additional tests to verify the flux density scale of our observations. First, comparing our GMRT data with the reprocessed 408 MHz all-sky survey of Haslam et al. (1981) – for the reprocessed data see Remazeilles et al. (2015) – we find the flux scale of our map to be consistent to within around 2 per cent. Secondly, we have analysed the data from our main secondary calibrator source, 0949+662.

4.1.4 Secondary calibrator: 0949+662

The principal secondary calibrator source[6] observed during this work was 0949+662 (J2000 right ascension and declination 09^{h}49^{m}12^{s}1 + 66°15$'$00$''$, respectively). This source is also known in the literature as 4C +66.09, and has been studied extensively in the radio band between 38 MHz and 30 GHz. We use previous measurements of the flux density to model the spectral energy distribution (SED) for this source and examine how the flux density recovered by the GMRT compares with established measurements. Flux density measurements from the literature are listed in Table 6, as well as the scaling factor required to bring the measurement into line with the SH12 flux density scale. Fig. 7 presents the flux density as a function of frequency for 0949+662.

The SED is modelled using a simple power-law spectral index between 38 MHz and 31.4 GHz. For 0949+662, the best-fitting spectral index is $\alpha = -0.33 \pm 0.03$. From Fig. 7, it is clear that there is some departure from a power law in the high-frequency regime ($\nu \gtrsim 10$ GHz). There also appears to be departure from power-law behaviour at low frequencies ($\nu \lesssim 74$ MHz) which may indicate self-absorption effects. Additional low-frequency observations would be required to investigate this further. The flux density recovered by the GMRT for 0949+662 is consistent with the power-law fit, and is also in agreement with the flux density measurement from the WENSS catalogue.

4.1.5 Source sizes

The observed spatial extent of a source may be estimated using the ratio of integrated flux density to peak flux density (for example Prandoni et al. 2000; Schinnerer et al. 2010; Hales et al. 2014b) via

$$\frac{S_{\text{int}}}{S_{\text{peak}}} = \frac{\theta_{\text{maj}}\theta_{\text{min}}}{B_{\text{maj}}B_{\text{min}}}, \tag{2}$$

where θ_{maj} and θ_{min} are the *observed* (i.e. not deconvolved) major and minor axes, respectively, and B_{maj} and B_{min} are the restoring beam major and minor axes FWHM. In the absence of image noise, unresolved sources have an integrated flux density equal to the peak flux density. However, image noise may affect the fit, and some unresolved sources may appear to have an integrated flux density that differs from the peak value.

In order to identify which sources are resolved and which are unresolved, we used the ratio of peak (S_{peak}) and integrated (S_{int}) flux density as a function of detection significance (i.e. $S_{\text{peak}}/\sigma_{\text{loc}}$). This is shown in Fig. 8. We define a locus that envelops 99.5 per cent of

---

[6] Selected from the VLA Calibrator Manual, available at http://www.aoc.nrao.edu/gtaylor/csource.html

Table 6. Flux density measurements from the literature for 0949+662 (4C +66.09), the principal secondary calibration source observed during this work, along with the native flux scale and the conversion factor required to bring the measurement on to the SH12 flux scale.

| Frequency (MHz)	S_{int} (Jy)	Flux scale	Factor	Catalogue reference
31 400	0.33 ± 0.10	B77	$-^a$	W78
30 000	0.27 ± 0.02	$-^b$	$-^b$	L07
10 695	0.77 ± 0.04	B77	1.027	K81
8400	0.78 ± 0.08^c	B77	1.021	P92
4900	1.23 ± 0.02	KPW	–	PT78
4850	1.41 ± 0.12	B77	1.007	BWE91
4850	1.40 ± 0.21^d	B77	1.007	GC91
4800	0.26 ± 0.03$^{c, e}$	VLBA^f	–	R05
2695	1.71 ± 0.08	B77	0.989	K81
2695	1.62 ± 0.02	B77	0.989	K81
1700	0.44 ± 0.04$^{c, e}$	VLBA^f	–	R05
1410	2.18 ± 0.01	B77	0.972	K81
1400	2.22 ± 0.22^c	B77	0.972	WB92
1400	2.30 ± 0.07	B77	0.972	C98
966	2.66 ± 0.27	KPW	–	C77
365	3.39 ± 0.05	TXS	0.977	D96
325	3.34 ± 0.17	SH12	–	SCG325
325	3.55 ± 0.18	WENSS^g	–	R97
178	3.32 ± 0.48^d	KPW	1.09	GSW67
151	4.06 ± 0.09	RBC73	–	H90
74	5.18 ± 0.52	B77	1.10	C07
38	4.40 ± 1.00^h	RBC73	–	C95

Notes. Flux scale notation: B77: Baars et al. (1977); KPW: Kellermann et al. (1969); RCB73: Roger et al. (1973); SH12: Scaife & Heald (2012); TXS: Douglas et al. (1996). Sources in the Texas radio survey were found to have flux densities that were consistent with a factor 0.9607 ×B77. References: BWE91: Becker, White & Edwards (1991); C77: Cohen et al. (1977); C95: Hales et al. (1995); C98: Condon et al. (1998); C07: Cohen et al. (2007); D96: Douglas et al. (1996); GC91: Gregory & Condon (1991); GSW67: Gower, Scott & Wills (1967); H90: Hales et al. (1990); K81: Kuehr et al. (1981); L07: Lowe et al. (2007); P92: Patnaik et al. (1992); PT78: Pauliny-Toth et al. (1978); R97: Rengelink et al. (1997); R05: Rossetti et al. (2005); SCG325: this work; W78: Witzel et al. (1978); WB92: White & Becker (1992).
^{a}30 GHz lies outside the frequency range covered by table 7 of Baars et al. (1977). We do not apply a correction factor. ^{b}The flux scale used by the observations of Lowe et al. (2007) was set using the calibrator source NGC 7027. We do not apply a correction factor. ^{c}We assume an uncertainty of 10 per cent. ^{d}The original uncertainty was quoted as 15 per cent of the integrated flux density. ^{e}The flux densities measured by the VLBA are 20 per cent of the total flux density at that frequency; here we quote the initial value, but in Fig. 7 we use the full flux density (i.e. 5 × this value). See Rossetti et al. (2005) for details. ^{f}The VLBA is the Very Long Baseline Array, located in the USA. We apply no correction factor to the VLBA measurements. ^{g}The WENSS flux scale is complex, depending on the sky position. We do not apply a correction factor to this source, see Section 4.1.3. ^{h}Multiple components exist at 38 MHz (Hales et al. 1995).

the sources with $S_{peak}/S_{int} > 1$, and mirrored this above $S_{peak} = S_{int}$, following the assumption that a similar number of unresolved sources will be scattered to $S_{peak}/S_{int} < 1$ by noise as those scattered to $S_{peak}/S_{int} > 1$. The locus was defined using the function

$$\frac{S_{peak}}{S_{int}} = k^{(S_{peak}/\sigma_{loc})^{-c}}, \quad (3)$$

where $k = 11.517$ and $c = 1.042$ provide the best fit to our data. All sources above this locus are considered to be resolved, and we use the integrated flux densities as recovered by PYBDSM in the SCG325
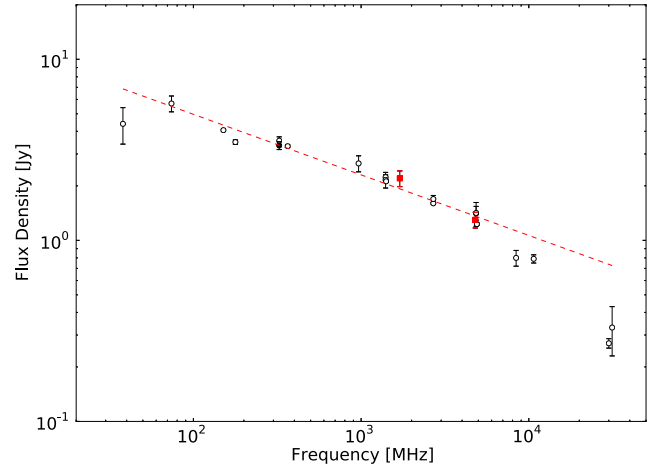
Figure 7. Flux density as a function of frequency for the principal secondary calibrator used in this work, 0949+662 (4C +66.09) between 38 MHz and 31.4 GHz. Open circles mark flux density measurements from the literature; filled squares mark flux densities measured with the VLBA, multiplied by a factor of 5 to show the total source flux density (see Rossetti et al. 2005). Filled circle indicates the flux density recovered by the GMRT. Dashed line indicates power-law fit to the spectral index between 38 MHz and 31.4 GHz, where $\alpha = -0.33 \pm 0.03$.
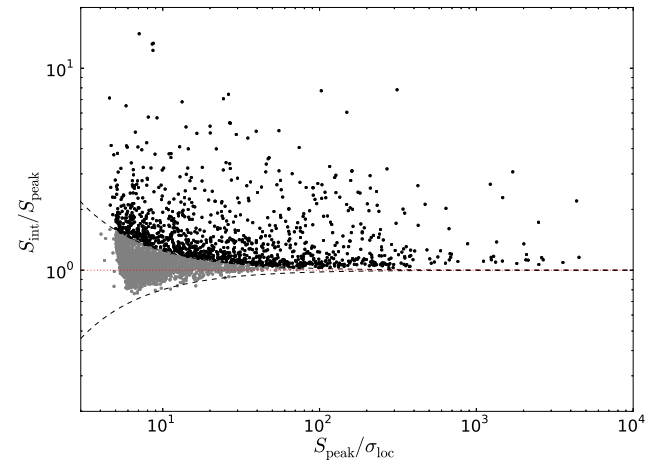

Figure 8. Ratio of integrated to peak flux density (S_{peak}/S_{int}) as a function of detection significance S_{peak}/σ_{loc} for sources in the SCG325 catalogue. Dotted line marks (S_{peak}/S_{int}) equal to unity. Dashed lines mark the locus used to differentiate resolved (black) and unresolved (grey) sources, defined by equation (3) and mirrored below $S_{peak} = S_{int}$.

catalogue. Sources below this locus are considered to be unresolved; we use the peak flux density in place of the integrated flux density when deriving the differential source counts in Section 6, and the angular size is undetermined. Following equation (3), 1207 sources in the SCG325 catalogue are considered to be resolved, and 2050 are unresolved. For resolved sources, we can estimate the deconvolved angular size via

$$\Theta \simeq \sqrt{\theta_{maj}\theta_{min} - B_{maj}B_{min}} \quad (4)$$

and we set the size of unresolved sources to zero. Unresolved sources have major and minor axes FWHM and position angles, as well as their associated uncertainties, denoted by '–' in Table 4.
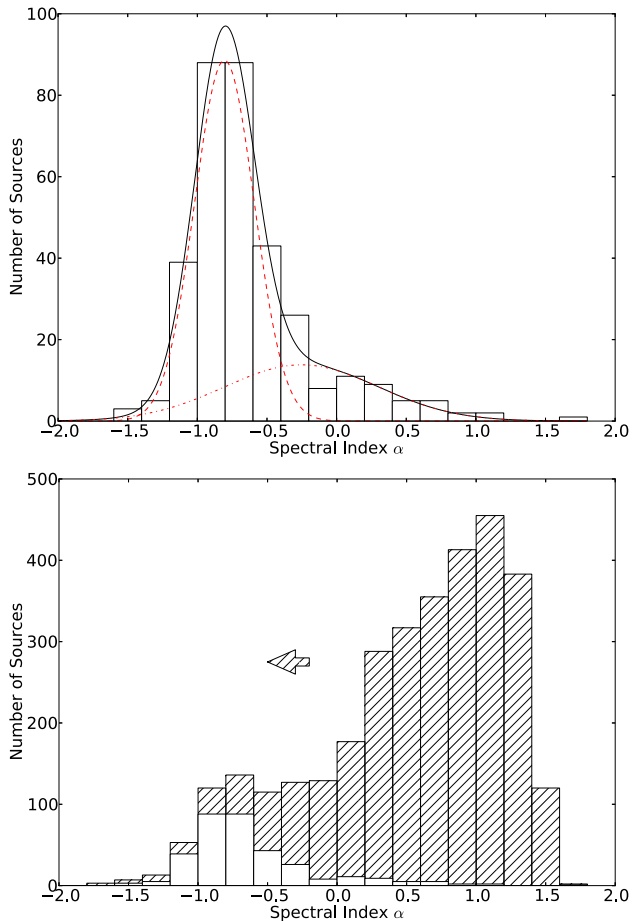
Figure 9. Source spectral index distribution between 1.4 GHz (from the NVSS catalogue) and 325 MHz (from this work). Top panel: spectral index estimates for sources with matches in the NVSS. The solid line indicates the combined best-fitting distribution, dashed (dot–dashed) lines indicate the Gaussians fitted to the steep-spectrum (flat-spectrum) population. The best-fitting models for these populations have peaks centred on $\alpha_1 = -0.81$ (dashed) and $\alpha_2 = -0.25$ (dot–dashed). Bottom panel: measured spectral index values for sources detected in the NVSS (no fill) and upper limits on the spectral index for sources without NVSS counterparts (hatched, and indicated by the arrow).

5 DISCUSSION

5.1 Spectral index distribution

For all sources with NVSS counterparts, we derive spectral index values using a simple power-law fit. We present the distribution of spectral index values between 325 and 1400 MHz in Fig. 9. From inspection, it is clear that the distribution is not well described by a single Gaussian. This suggests that two populations exist within this distribution: a larger population of sources centred around a spectral index of −0.8 (typical of synchrotron-dominated emission) and a smaller population of sources with flat or rising spectra. We note that this distribution is biased due to the limited sensitivity of the NVSS observations used as the higher frequency reference; as such we also include upper limits to the spectral index for sources without NVSS counterparts in the lower panel of Fig. 9.

Subsequently, we fit two Gaussian functions to this distribution. The best fit yields distributions with mean spectral index $\alpha_1 = -0.81 \pm 0.21$ for the steep-spectrum population and $\alpha_2 = -0.25 \pm$

0.55 for the flat-spectrum population. These population distributions are also indicated in Fig. 9.

The mean spectral index of the dominant source population within the SCG325 catalogue is consistent with that derived in previous work (for example, Mauch et al. 2013; Smolčić et al. 2014). Fig. 11 of Sirothia et al. (2009) presents the histogram of spectral index values for the sources in the ELAIS-N1 field, which appears to exhibit marginal evidence of a small, rising-spectrum population alongside the dominant population. Mauch et al. (2013) find a spectral index distribution that is well described by a single Gaussian centred on $\alpha = -0.71$. This difference is naturally explained by the difference in sensitivity between the observations in this work (nominal sensitivity 34 μJy beam^{-1}) and the work of Mauch et al. (where the nominal sensitivity was ∼1–7 mJy beam^{-1}). The deeper observations presented here recover sources with flux densities far below 1 mJy; a regime where the contribution from SFG and RQ-AGN become increasingly important (for example Prandoni et al. 2001; Padovani et al. 2007, 2009, 2015; Smolčić et al. 2008; Ibar et al. 2009).

However, the spectral index distribution presented in Fig. 9 is unlikely to be probing the population of SFG in this field. With only 335 spectral index estimates out of a catalogue of 3257 sources, the spectral index distribution we have derived is severely limited by the sensitivity of the NVSS catalogue; the NVSS catalogue is limited to sources of flux densities in excess of ∼2–3 mJy, whereas SFG typically dominate below 0.1–1 mJy at 1.4 GHz. Hence, the population of flat-/rising-spectrum sources in the SCG325 catalogue may be comprised of a number of different source types – the brighter sources may be flat-spectrum radio quasars (FSRQ) or blazars; some of the fainter flat-spectrum sources may be core-dominated AGN (Randall et al. 2012) or hybrid sources exhibiting both star formation and a central engine (for example, Hill et al. 1999; Hill et al. 2001). Alternatively some of these flat spectra may be attributed to absorption effects in the local environment. Further observations at other frequencies are required to discriminate between scenarios. A detailed investigation of the nature of this flat-spectrum population will form the subject of future work, as the highly sensitive 1.4 GHz data required are currently being taken with e-MERLIN and the JVLA.

5.1.1 Relation between spectral index and flux density

We present the dependence of the spectral index on the 325 MHz integrated flux density in Fig. 10. There is significant bias in Fig. 10 due to the sensitivity limit of the NVSS; this is indicated by the solid line in Fig. 10, and cuts out a large region of the parameter space. In some previous works, there has been a detection of a 'flattening' in the spectral index distribution below $S_{1.4\,\text{GHz}} = 10$ mJy (for example, Prandoni et al. 2006; Mignano et al. 2008) whereas other authors do not detect such a feature (for example, Ibar et al. 2009; Randall et al. 2012). Randall et al. (2012) suggest that this flattening may be associated with a population of core-dominated AGN at the faintest flux densities; as such, the mean spectral index flattens to $\alpha > -0.7$.

The picture from studies of the low-frequency spectral index is also mixed. Fig. 13 of Sirothia et al. (2009) exhibits marginal evidence of a flattening in the region 1–10 mJy, whereas Tasse et al. (2006) and Mauch et al. (2013) find 'little-to-no evidence' of this. Again, sensitivity differences provide a natural explanation for this. From Fig. 10 there is also marginal evidence of this flattening in the spectral index/flux density relation in the 1–10 mJy region. With a sample size of 335 out of a total catalogue of 3257 sources, more
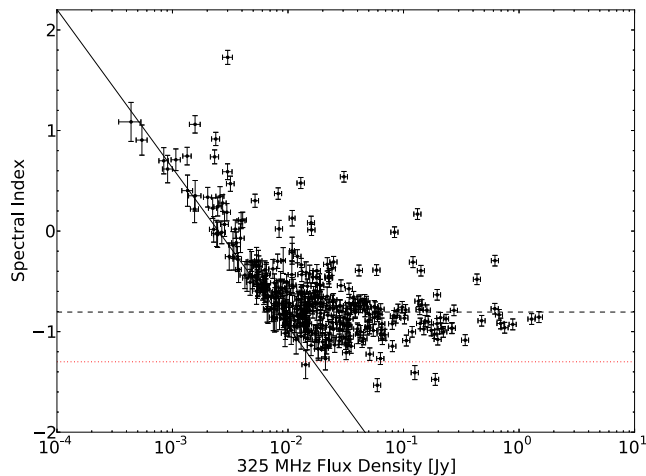
Figure 10. Spectral index as a function of 325 MHz flux density for the 335 sources in the SCG325 catalogue which have counterparts detected in the NVSS. Solid sloping line marks the flux density traced by the nominal NVSS detection limit of 2.5 mJy. Dashed line marks mean spectral index of the dominant population. Dotted line marks nominal 'steep spectrum' index of $\alpha = -1.3$.

sensitive observations of this region are required at higher frequency to better examine any relationship between flux density and spectral index and confirm whether this flattening is a real feature or simply due to sample bias.

5.2 USS sources

USS radio sources are often associated with radio galaxies at high redshift (HzRGs). Studies have shown that these are among the most luminous and massive galaxies (for example, De Breuck et al. 2005; Seymour et al. 2007; Singh et al. 2014) and are believed to be progenitors of the massive elliptical galaxies in the local Universe. These have also been shown to be associated with overly dense regions of space: galaxy clusters and protoclusters at redshifts $z \sim 2-5$ (for example, Stevens et al. 2003; Venemans et al. 2007; Casey et al. 2015; Diener et al. 2015). Identifying and studying HzRGs enables us to better understand the mechanisms by which these sources form and evolve in dense environments and at high-z. Most HzRG sources at $z \gtrsim 3$ have been identified through detection of USS radio sources, which are bright at low frequencies and often appear compact (for example, Klamer, Ekers & Hunstead 2007; Miley & De Breuck 2008).

We find two sources with spectral index more than $3\sigma_1$ below the mean spectral index of the dominant population (i.e. $\alpha < -1.45$) which we investigate as USS sources. In the literature, USS radio sources are commonly defined as those with spectral index values $\alpha < -1.3$. We find a further two sources which satisfy this condition, for a total of four ultrasteep spectrum candidates (USSc). Postage stamp images of these sources are presented in Fig. 11. In Table 7, we list the integrated flux densities at 325 MHz (from this work) and 1400 MHz (from the NVSS) and the two-point spectral index values. In this section, we discuss these sources and cross-reference them with the literature.

5.2.1 SCG325_J101231+680942

This source has been identified in a number of previous radio surveys; for example in the NVSS its identifier is NVSS

J101231+680940. Additional flux density measurements for this source exist at 38, 74, 151 and 325 MHz, from a number of historic radio surveys. These flux density measurements are listed in Table 8, with the appropriate correction factor required to bring them into line with the SH12 flux density scale. Subsequently, we use the corrected flux densities to fit a spectral index in the form of a power law between 38 MHz and 1.4 GHz. We present the flux density as a function of frequency in the top panel of Fig. 12, as well as the spectral index fitted to the data from the literature, $\alpha = -1.27 \pm 0.22$. This fit suggests a spectral index that is marginally shallower than the two-point spectral index indicated in Table 7.

Based on the multifrequency spectral index, we cannot conclusively say whether this source has a USS; from Fig. 12, the integrated flux density recovered by the GMRT appears to be in excess of that expected from the flux density measurements in the literature. However, from Fig. 11 (top panel) it appears that this source is extended at the resolution of the GMRT, so it is possible that this excess is a result of the superior sensitivity to faint emission compared to previous surveys.

5.2.2 SCG325_J102419+671742

SCG325_J102419+671742 (also known as 8C 1020+675) has been identified in a number of previous radio surveys between 38 MHz and 1.4 GHz. From Fig. 11 (bottom panel) it is extended at both the resolution of the GMRT and NVSS. Historic values of the flux density for 8C 1020+675 are presented in Table 8, with their associated flux scale and the conversion factor necessary to make them consistent with the SH12 flux scale.

Fig. 12 (bottom panel) also presents the flux density as a function of frequency for this source, along with the multifrequency spectral index fit. We model the spectral index behaviour of 8C 1020+675 as a power law between 38 MHz and 1.4 GHz, deriving a spectral index of $\alpha = -1.31 \pm 0.26$. While this is marginally flatter than the two-point fit listed in Table 7 ($\alpha = -1.41 \pm 0.07$) it is sufficiently steep to qualify as a USS radio source. The flux density recovered by the GMRT is in good agreement with the multifrequency fit to measurements from the literature.

The postage stamp image of 8C 1020+675 presented in Fig. 11 (lower panel) reveals a complex morphology, with extended radio emission on angular scales up to ∼120 arcsec. A pair of potential optical hosts are identified in the DSS, although they lie towards the southern tail of the radio emission. This source also appears to be coincident with the object GALEXASC J102418.81+671744.1. No redshift measurements are available in the literature so we cannot confirm its size. Detailed optical analysis of this field is underway and may shed further light on the nature of this source.

5.2.3 Other steep-spectrum candidates

As can be seen in Fig. 11, SCG325_J101808+665632 and SCG325_J102253+672121 (panels two and three, respectively) appear reasonably compact at the resolution of the GMRT. SCG325_J101808+665632 has the steepest spectrum of all sources with NVSS counterparts ($\alpha = -1.53 \pm 0.06$) and is reasonably bright at 325 MHz (an integrated flux density $S = 59.30 \pm 4.23$ mJy). These sources have not been detected in any other historic radio surveys, so their steep spectra cannot yet be independently confirmed; likewise no redshift measurements exist, so we cannot yet investigate whether these may be HzRGs. However, being both bright and compact, they present themselves as promising candidates.
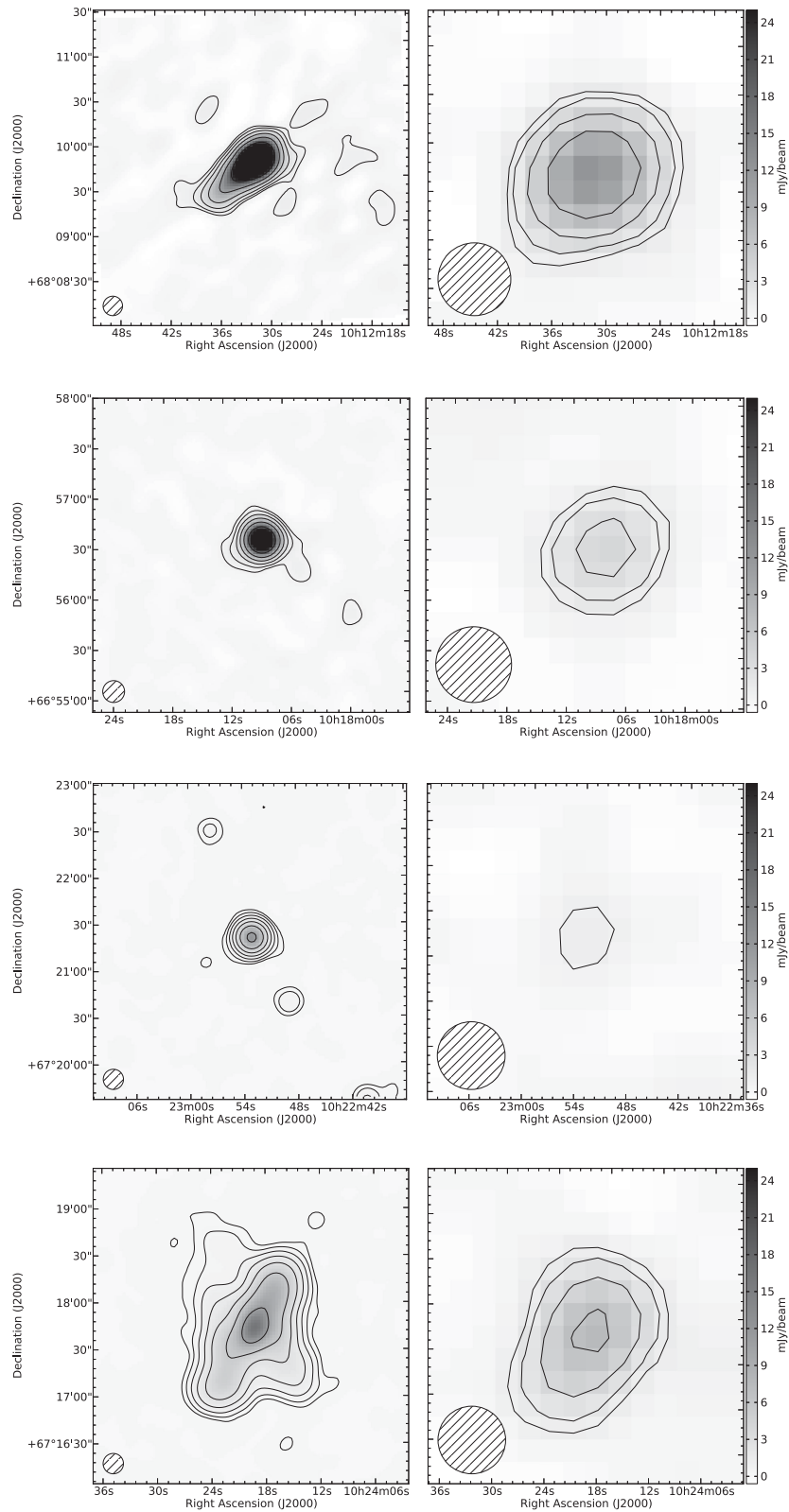
Figure 11. Candidate USS radio sources from the SCG325 catalogue. From top to bottom: SCG325_J101231+680942, SCG325_J101808+665632, SCG325_J102253+672121, SCG325_J102419+671742. Left-hand panels: GMRT images. Contours start at $5\sigma_{local}$ and scale by a factor of 2, where the local noise $\sigma_{local} = 140 / 125 / 36 / 35$ μJy beam^{-1} from top to bottom. Right-hand panels: postage stamp from the NVSS at 1.4 GHz. First contour is at $3\sigma_{nom}$, then scale by a factor of 2 from $5\sigma_{nom}$ where σ_{nom} is the nominal NVSS image noise of 0.5 mJy beam^{-1}. Images are set to matching colour scales and saturate at 25 mJy beam^{-1}. Beam sizes are indicated by the hatched circle in the lower-left corner.

Table 7. USS sources and GPS sources from the SCG325 catalogue that have been selected for further study. Integrated flux densities at 1.4 GHz are from the NVSS, and have been corrected by a factor of 0.972 to bring them on to the SH12 scale. We quote alternative names from the literature where they exist; the NVSS source identification if no others exist.

Name	RA (J2000) h:m:s	DEC (J2000) $\circ$:′:″	S_{int}(325 MHz) (mJy)	S_{int}(1.4 GHz) (mJy)	α	Alternate name
SCG325_J101231+680942	10 12 31.47	68 09 42.5	188.44 ± 13.35	21.87 ± 1.07	-1.48 ± 0.06	NVSS J101231+680940
SCG325_J101808+665632	10 18 08.51	66 56 32.8	59.30 ± 4.23	6.32 ± 0.39	-1.53 ± 0.06	NVSS J101808+665632
SCG325_J102253+672121	10 22 53.05	67 21 21.1	14.21 ± 1.01	2.04 ± 0.39	-1.33 ± 0.14	NVSS J102253+672118
SCG325_J102419+671742	10 24 19.15	67 17 42.5	125.37 ± 8.88	16.04 ± 1.17	-1.41 ± 0.07	8C 1020+675
SCG325_J101418+683826	10 14 18.30	68 38 26.5	12.91 ± 0.95	25.95 ± 0.87	$+0.48 \pm 0.06$	NVSS J101418+683826
SCG325_J101538+672844	10 15 38.12	67 28 44.8	3.01 ± 0.29	37.52 ± 1.17	$+1.73 \pm 0.07$	CGRaBS J1015+6728
SCG325_J101723+673633	10 17 23.75	67 36 33.3	30.51 ± 2.17	67.17 ± 2.04	$+0.54 \pm 0.05$	87 GB 101339.1+675144
SCG325_J103401+683226	10 34 01.15	68 32 26.6	132.14 ± 9.37	169.03 ± 5.05	$+0.17 \pm 0.05$	87 GB 103023.1+684757

It should be noted that we have only examined sources which have counterparts in the NVSS. As such, our current sample of USS sources is severely limited, and many more steep-spectrum objects may be present in the field. The highly sensitive e-MERLIN and JVLA data being taken may reveal an increased population of very steep spectrum objects, and will allow us to study the ones identified here in more detail. Additionally, a deep optical study of this region is underway as part of ancillary science work, which may provide insight into whether these sources may be HzRGs.

5.3 Flat-/rising-spectrum Sources

A source may possess a flat/rising radio spectrum for a number of reasons – bright sources with rising spectra may be high-redshift quasars or blazars, whereas faint flat-spectrum sources may be SFG. A rising low-frequency radio spectrum is usually associated with synchrotron emission from a relativistic electron population as modified by absorption processes. This may be for example free–free absorption (FFA) by a warm gas environment, or synchrotron self-absorption (SSA) of the radio-emitting electrons.

Given the sensitivity limits of the high-frequency reference, it is unlikely that any of these sources are SFG. Instead, this sample better fits the description of GPS sources. GPS radio sources are a type of AGN whose radio emission peaks at GHz frequencies, usually exhibiting a sharp drop-off either side of the turnover frequency. These sources are typically compact in nature ($\sim$0.1–1 kpc in extent) with low polarization fraction and generally exhibit little variability over long time-scales (O'Dea, Baum & Stanghellini 1991). For comprehensive reviews of GPS radio sources, see O'Dea (1998), Stawarz et al. (2008) or Marr et al. (2014).

Of the 335 sources common to both the SCG325 and NVSS catalogues, 42 sources have spectral index values $\alpha > -0.16$ (the $3\sigma_1$ limit of the steep-spectrum population). By inspection, no spatial trend in their distribution is apparent – these sources appear to be fairly evenly scattered across the survey area. From Fig. 10 we identify sources with reliably steep, rising spectra for further analysis, as well as a number of reasonably bright sources with positive spectral indices, for a total of four GPS candidates. The identifiers for these sources, their right ascension and declination, as well as the flux densities at 325 and 1400 MHz, and the two-point spectral index, are also listed in Table 7. These selected sources all appear compact at the resolution of the GMRT; as a result, we do not present postage stamp images in this work. The first of these, SCG325_J101418+683826 does not appear in any other catalogues besides the NVSS, and cannot yet be investigated further. In this section, we investigate the remainder of this GPS sample.

5.3.1 SCG325_J101538+672844

We find a single source with a spectral index more than $3\sigma_2$ above the mean spectral index (α_2) of the flat-spectrum population (i.e. a steep rising spectrum). The two-point spectral index of this source is $\alpha = 1.73 \pm 0.07$. This source has also been identified in the literature in a number of high-frequency radio surveys; for example, one identifier is CGRaBS J1015+6728 (Healey et al. 2008). We present the flux densities listed in other catalogues, alongside the conversion factor required to bring them on to the SH12 flux density scale in Table 8.

Previous work suggests that CGRaBS J1015+6728 is a blazar; flux density measurements from the literature between 1.4 and 15 GHz indicate a rising spectrum with a turnover at higher frequencies (see Table 8). We recover an integrated flux density of 3.09 ± 0.31 mJy; a value that appears consistent with this behaviour. To our knowledge, this is the first flux density measurement for this source below 1 GHz. Whilst the SED of CGRaBS J1015+6728 does not show any obvious signs of variability (see the top panel of Fig. 13) the OVRO data base[7] indicates that this source has been increasing in flux density steadily since monitoring observations began in 2009.

5.3.2 SCG325_J101723+673633

This source is also known in the literature as 87 GB 101339.1+675144. Observations of this source have been performed over the course of several decades. From Fig. 13 (centre panel) the flux density measurements appear to be reasonably stable, at least over a period of several years. However, all measurements of the flux density at 4.85 and 8.4 GHz were taken in the period 1986–1999; more recent observations at higher frequencies are required to test the variability on longer time-scales. At low frequencies, there is a discrepancy between the flux densities from this work and from WENSS; this may be due to intrinsic variability, or alternatively may be due to the general scatter in flux density ratio between the SCG325 and WENSS catalogues at low flux densities.

5.3.3 SCG325_J103401+683226

This source is also known in the literature as 87GB 103023.1+684757, and has been the subject of a number of observations since the 1980s. From Fig. 13 (lower panel) it appears that the spectrum of SCG325_J103401+683226 is approximately flat

---

[7] Available online at http://www.astro.caltech.edu/ovroblazars/

Table 8. Flux density measurements from this work and the literature for USS and GPS radio sources identified in this work (see Table 7). The 'Factor' column indicates the correction assumed to bring the flux density measurement on to the SH12 flux scale.

Source	Source type	Frequency (MHz)	S_{int} (mJy)	Flux scale	Factor	Catalogue
SCG325_J101231+680942 (NVSS J101231+680940)	USS	1400	22.5 ± 1.1	B77	0.972	NVSS (Condon et al. 1998)
		325	153 ± 31	WENSS	–	WENSS (Rengelink et al. 1997)
		325	188.4 ± 13.4	SH12	–	SCG325 (this work)
		151	350 ± 40	RCB73	–	6C (Hales et al. 1990)
		151	438 ± 88	RCB73	–	7C (Hales et al. 2007)
		74	780 ± 100	B77	1.10	VLSS (Cohen et al. 2007)
		38	2400 ± 1000	RCB73	–	8C (Hales et al. 1995)
SCG325_J102419+671742 (8C 1020+675)	USS	1400	16.5 ± 1.2	B77	0.972	NVSS (Condon et al. 1998)
		325	132.1 ± 9.4	SH12	–	SCG325 (this work)
		325	87 ± 17	WENSS	–	WENSS (Rengelink et al. 1997)
		232	310^a	RCB73	–	Miyun (Zhang et al. 1997)
		151	330 ± 40	RCB73	–	6C (Hales et al. 1990)
		74	600 ± 80	B77	1.10	VLSS (Cohen et al. 2007)
		38	1500 ± 700	RCB73	–	8C (Hales et al. 1995)
SCG325_J101538+672844 (CGRaBS J1015+6728)	GPS	15000	105.0 ± 1.0	B77	1.035	OVRO Blazar Monitoring Program; (Richards et al. 2011)
		8400	150.1 ± 15.0^b	B77^c	1.021	CGRaBS (Healey et al. 2008)
		8400	146.1 ± 14.6^b	B77^c	1.021	Becker et al. (1991)
		4850	117.0 ± 11.0	B77^d	1.007	Gregory & Condon (1991)
		1400	39.1 ± 1.3	B77	0.972	NVSS (Condon et al. 1998)
		325	3.1 ± 0.3	SH12	–	SCG325 (this work)
SCG325_J101723+673633 (87GB 101339.1+675144)	GPS	8400	19.3 ± 0.2	B77^c	1.021	JVAS/CLASS (Jackson et al. 2007)
		8400	20.4 ± 2.0^b	B77	1.021	VLA-CLASS (Myers et al. 2003)
		4850	38.0 ± 3.8^b	B77	1.007	Becker et al. (1991)
		4850	41.0 ± 6.0	B77	1.007	87GB (Gregory & Condon 1991)
		4850	35.0 ± 4.0	B77	1.007	GB6 (Gregory et al. 1996)
		1400	69.1 ± 2.1	B77	0.972	NVSS (Condon et al. 1998)
		325	22.0 ± 3.8	WENSS	–	WENSS (Rengelink et al. 1997)
		325	30.5 ± 2.2	SH12	–	SCG325 (this work)
SCG325_J103401+683226 (87GB 103023.1+684757)	GPS	8400	103.7 ± 1.0	B77^c	1.021	JVAS/CLASS (Jackson et al. 2007)
		8400	110.9 ± 11.1^b	B77^c	1.021	CRATES (Healey et al. 2007)
		8400	111.0 ± 11.1^b	B77	1.021	(Patnaik et al. 1992)
		5000	$105.5 \pm 10.6^{b,\,e}$	B77	1.007	MASIV (Lovell et al. 2008)
		4850	151.0 ± 13.0	B77	1.007	87GB (Gregory & Condon 1991)
		4850	154.0 ± 14.0	B77	1.007	GB6 (Gregory et al. 1996)
		1400	173.9 ± 5.2	B77	0.972	NVSS (Condon et al. 1998)
		325	88.0 ± 5.7	WENSS	–	WENSS (Rengelink et al. 1997)
		325	132.1 ± 9.4	SH12	–	SCG325 (this work)

Notes. Flux scale notation: B77: Baars et al. (1977) , RCB73: Roger et al. (1973), SH12: Scaife & Heald (2012).
^{a}The given flux density for 8C 1020+675 from the Miyun survey is the peak flux density, rather than integrated flux density. We exclude this value from Fig. 12, but it is quoted here for completeness. ^{b}We have assumed a 10 per cent uncertainty in this measurement. ^{c}Flux scale is consistent with the VLA-CLASS survey. ^{d}Flux scale is within 2 per cent of the B77 scale. ^{e}This source was observed on four occasions in 2002–2003, recovering integrated flux densities of 104, 106, 107 and 105 mJy (see Lovell et al. 2008). We quote the mean flux density here.

between 325 MHz and 8.4 GHz, with signs of variation at high frequencies. Flux density measurements in the 5–8 GHz range appear to be approximately consistent for data taken between 1986–1990 (Gregory & Condon 1991; Patnaik et al. 1992; Gregory et al. 1996) and 1994–1999 (Healey et al. 2007). More recent observations from the 2002–2003 period perhaps suggest variation on longer time-scales, as the flux density has been observed to decrease at 5 GHz (Lovell et al. 2008).

At lower frequencies, there is a discrepancy in the flux density recovered by the WENSS and this work. For this source, the GMRT recovers flux density in excess of the WENSS by approximately 50 per cent. This may be explained by intrinsic variability, although the general scatter in the flux density ratio between the SCG325 and WENSS catalogues at low flux densities may have some contribution to this difference.

5.3.4 Modelling

Previous work on GPS sources has often attempted to discriminate between single/multiple-component SSA/FFA models in cases where large numbers of flux density measurements across multiple frequencies exist (for example, Callingham et al. 2015). For the GPS sources discussed in this work, however, there are insufficient measurements in the literature to conduct a thorough investigation. Hence, using all available data from the literature, as presented in Table 8, as well as the new flux density measurements from the SCG325 catalogue, we model these GPS sources using a simple broken power-law fit of the form

$$S\ [\text{mJy}] = \begin{cases} A_0 \nu^{\alpha_{\text{lo}}} & : \nu < \nu_{\text{crit}} \\ B_0 \nu^{\alpha_{\text{hi}}} & : \nu \geq \nu_{\text{crit}}, \end{cases}$$
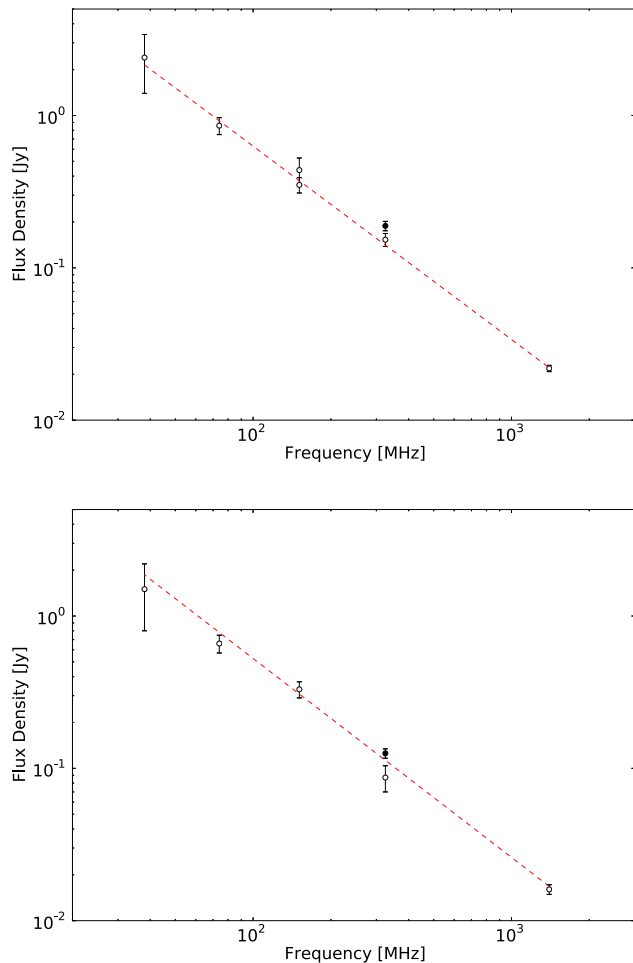
Figure 12. Flux density as a function of frequency for SCG325_J101231+680942 (NVSS J101231+680940; top panel) and SCG325_J102419+671742 (8C 1020+675; bottom panel) between 38 MHz and 1.4 GHz. Filled (open) circles indicate flux density measurements from this work (the literature). Dashed lines indicate the fitted multifrequency spectral index $\alpha = -1.27 \pm 0.22$ (-1.31 ± 0.26) in the top (bottom) panel.

where α_{lo} and α_{hi} are the low-/high-frequency spectral index, respectively, and ν_{crit} is the turnover frequency. The fitted spectral index values (α_{lo} and α_{hi}) are listed in Table 9, as well as the turnover frequency. In future, when the wide-band JVLA and LOFAR data become available, we should be able to investigate the validity of single-/multiple-component SSA/FFA models as the mechanism responsible for the shape of the SED.

We present SEDs for these sources in Fig. 13 as well as the fitted broken power-law spectral index models. For SCG325_J101538+672844, α_{hi} is consistent with an essentially flat spectral index above around 3 GHz, whereas α_{lo} is strongly indicative of absorption processes, perhaps FFA or SSA, which presents with a typical spectral index of around $\alpha \simeq 2.5$. However, from previous work (for example, Muxlow et al. 2005; Fomalont et al. 2006; Owen & Morrison 2008) the size of quasars and beamed radio sources is typically $\sim$1 arcsec, whereas SSA requires scale sizes of $\ll$ mas size (Owen et al. 2009 and references therein). The resolution of these GMRT data do not allow us to differentiate between these scenarios; the higher resolution data being taken with other instruments may allow us to better investigate the mechanism responsible for the shape of these spectra.
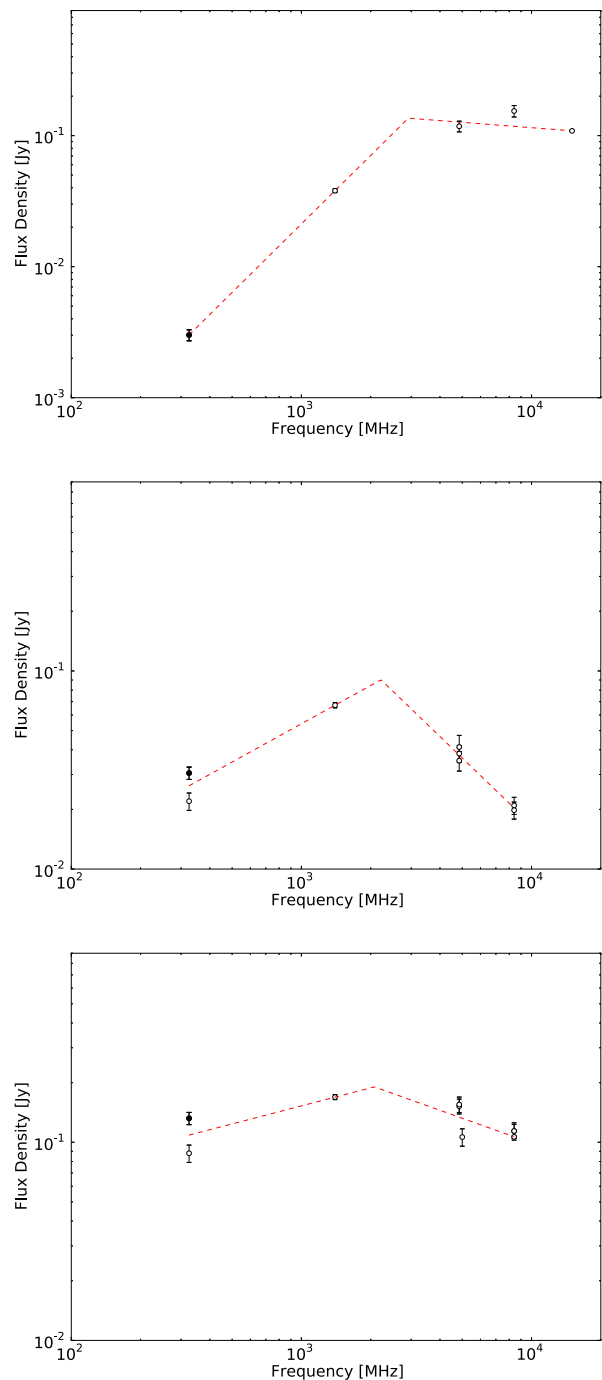
Figure 13. SEDs for GPS sources identified from the SCG325 catalogue. Top: SCG325_J101538+672844 (CGRaBS J1015+6728). Centre: SCG325_J101723+673633 (87GB 101339.1+675144). Bottom: SCG325_J103401+683226 (87GB 103023.1+684757). Filled (open) circles mark data from this work (the literature) as presented in Table 8, with appropriate correction factors applied. Dashed lines denote the broken power law fits to the data, from Table 9.

6 SOURCE COUNTS

Source counts as a function of flux density have been extensively studied at 1.4 GHz (for example, Mitchell & Condon 1985; Windhorst et al. 1985; White et al. 1997; Hopkins et al. 2003; Huynh et al. 2005; Bondi et al. 2008) and a number of frequencies below 1 GHz (for example, Wieringa 1991; Garn et al. 2008a,b; Owen

Table 9. Fitted spectral index models for rising-spectrum sources.

Source	α_{lo}	α_{hi}	ν_{crit} (GHz)
SCG325_J101538+672844	1.74 ± 0.17	-0.14 ± 0.18	2.92 ± 0.17
SCG325_J101723+673633	0.64 ± 0.07	-1.12 ± 0.26	2.22 ± 0.16
SCG325_J103401+683226	0.30 ± 0.10	-0.41 ± 0.22	2.07 ± 0.35

et al. 2009; Sirothia et al. 2009; Mauch et al. 2013; Smolčić et al. 2014).

It is well established that the Euclidean-normalized source counts distribution at 1.4 GHz exhibits a flattening at around 1 mJy; this has been seen in observations at 610 MHz and 325 MHz (see de Zotti et al. 2010 for a review of radio surveys across a wide range of frequencies). A subsequent downturn towards fainter flux densities (100−150 μJy at 1.4 GHz) has also been suggested by Bondi et al. (2008). Assuming a typical synchrotron spectral index of $\alpha = -0.7$, this corresponds to a flux density of around 180−250 μJy at 610 MHz, or 300−400 μJy at 325 MHz. This suggests that the majority of previous surveys at low frequencies have had insufficient sensitivity to confirm/refute this feature.

However, in this work, we recover sources with flux densities down to 183 μJy, which suggests we possess sufficient sensitivity to investigate this further. In this section, we discuss the process by which we derive our source counts alongside our treatment of resolution bias and Eddington bias, as well as cosmic variance. Subsequently we analyse the Euclidean-normalized differential source counts distribution derived from the SCG325 catalogue.

### 6.1 Construction of source counts

Sources were binned according to their integrated flux density, adopting the binning strategy of Hales et al. (2014a). As such, bin widths were set at 0.07 dex for $S < 1$ mJy, 0.13 dex for 1 mJy $\leq S < 10$ mJy, and 0.2 dex for $S \geq 10$ mJy. Subsequently, bins were optimized to achieve raw counts (N) of at least 9, and hence maintain a signal-to-noise ratio of at least 3. Given that all sources in our catalogue exceed a flux density of 183 μJy, all our bins are in excess of five times the nominal image noise.

The corrected number of sources in a given flux density bin, N_c, was found by first deriving the image area detection fraction for each source in our catalogue. This was done using the effective noise image, which is derived from the measured noise (presented in Fig. 2) divided by the local bandwidth smearing ratio (see equation 8 later). The detection fraction as a function of source flux density is presented in Fig. 14, where the black points indicate the detection fraction for the mean flux density in a given bin. Subsequently, N_c is derived by

$$N_c = \sum_{nsrc} (V_{area})^{-1},\qquad(5)$$

where V_{area} is the image detection area for a given source. Note that from Fig. 14 the faintest bin (183−223 μJy) has a very small image area detection fraction (and therefore a high area correction factor). As such, this bin was excluded from further analysis, as the sources in this bin would only be detected over a very small (and perhaps unrepresentative) region of our survey.

The differential source counts $n(S) = dN/dS$ were then calculated by dividing the corrected number of sources in each bin, N_c, by $A\Delta S$, where A is the image area (in steradians) and ΔS is the bin width (in Jy). We derived the source counts using the full image
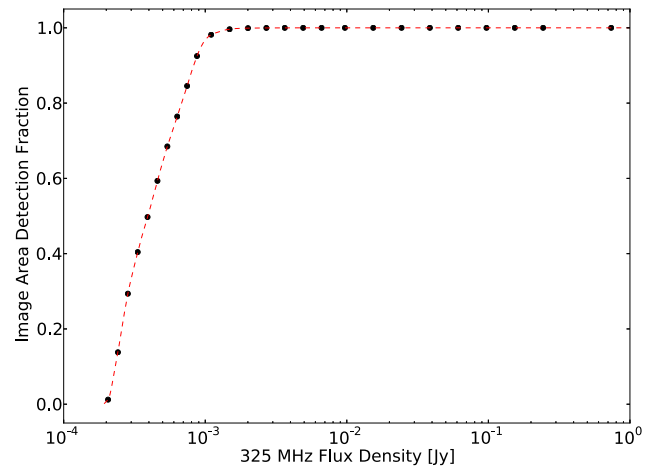
Figure 14. Image area correction factor as a function of flux density at 325 MHz. Black points mark the mean flux density of bins, red dashed line marks the per-source image detection fraction.

area, approximately 6.5 deg^2 (0.002 sr). The bins, raw counts, corrected counts, differential source counts, and Euclidean-normalized differential source counts $n(S) S^{2.5}$, are presented in Table 10. The Euclidean normalization is performed using the geometric mean flux density, S_c, of sources in each bin. We have assumed Poisson statistics in deriving the errors on the source counts. The differential source counts presented in Table 10 have been corrected for both resolution bias and Eddington bias, as described in the following sections.

6.2 Cosmic variance

We can estimate the effect of cosmic variance using the work of Heywood, Jarvis & Condon (2013). With a survey area of ∼6.5 deg^2, this is the widest deep-field yet studied at 325 MHz; as such we would expect the least uncertainty due to cosmic variance. Assuming a spectral index $\alpha = -0.7$, and given the field of view over which the source counts were derived we would expect the uncertainty introduced by cosmic variance effects to be of the order of 1–3 per cent at the flux density limit of this survey; a value small compared to other uncertainties.

6.3 Resolution bias

Given that source catalogues are compiled using detection algorithms are largely based on identification of sources at a given significance above the noise level – i.e. based on peak flux density – whereas source counts are derived using the integrated flux density, the resolution of a survey can significantly impact the recovered source counts. At increasingly high resolution, surveys may resolve out sources that possess low surface brightness, but are sufficiently large that their integrated flux density would contribute to the source counts distribution.

Recent work by (Hales et al. 2014b, hereafter H14) has provided a robust formalism for estimating the correction required to account for resolution bias. H14 include two effects under the resolution bias umbrella: first, the incompleteness due to lack of sensitivity to resolved low surface brightness sources, and secondly the redistribution of source counts between bins as a result of underestimating flux densities for unresolved sources. This second component of resolution bias was identified by Bondi et al. (2008). In this section,

Table 10. Differential source counts at 325 MHz. The differential source counts and Euclidean-normalized differential source counts quoted here have all been corrected for image area detection fraction, resolution bias and Eddington bias.

Flux bin (mJy)	S_c (mJy)	N	N_c	$\frac{dN}{dS}$ (Jy^{-1} sr^{-1})	$\frac{dN}{dS} S_c^{2.5}$ (Jy$^{1.5}$ sr^{-1})
0.223–0.262	0.242	114	877.5	1.37×10^{10}	12.49 ± 0.42
0.262–0.308	0.284	198	697.7	9.01×10^9	12.26 ± 0.46
0.308–0.361	0.333	242	605.6	7.06×10^9	14.33 ± 0.58
0.361–0.424	0.391	255	511.0	5.11×10^9	15.48 ± 0.68
0.424–0.498	0.460	237	401.5	3.37×10^9	15.24 ± 0.76
0.498–0.585	0.540	224	329.6	2.32×10^9	15.72 ± 0.87
0.585–0.687	0.634	200	262.8	1.55×10^9	15.73 ± 0.97
0.687–0.807	0.745	206	244.3	1.21×10^9	18.37 ± 1.18
0.807–0.948	0.875	183	198.1	8.35×10^8	18.88 ± 1.34
0.948–1.279	1.10	309	316.0	5.60×10^8	22.55 ± 1.27
1.279–1.725	1.49	229	230.1	3.01×10^8	25.58 ± 1.69
1.725–2.327	2.00	166	166.2	1.56×10^8	28.09 ± 2.18
2.327–3.139	2.70	122	122.0	8.32×10^7	31.61 ± 2.86
3.139–4.234	3.65	105	105.0	5.22×10^7	41.89 ± 4.09
4.234–5.712	4.92	85	85.0	3.09×10^7	52.37 ± 5.68
5.712–7.705	6.63	61	61.0	1.63×10^7	58.26 ± 7.46
7.705–12.21	9.70	76	76.0	8.86×10^6	82.08 ± 9.42
12.21–19.35	15.41	79	79.0	5.75×10^6	168.5 ± 19.0
19.35–30.67	24.36	51	51.0	2.32×10^6	215.2 ± 30.1
30.67–48.61	38.61	30	30.0	8.57×10^5	251.1 ± 45.8
48.61–77.04	61.20	20	20.0	3.52×10^5	325.8 ± 72.9
77.04–122.1	97.0	16	16.0	1.78×10^5	520.0 ± 130.0
122.1–193.5	153.7	14	14.0	9.80×10^4	908.0 ± 242.7
193.5–306.7	243.6	9	9.0	3.97×10^4	1164.3 ± 388.1
306.7–1770.8	737.0	11	11.0	3.76×10^3	1751.2 ± 528.0

we will closely follow the method of H14 to derive the correction for resolution bias.

6.3.1 Effect 1: sensitivity to resolved sources

In our work, we possess modest resolution (13 arcsec) and use a weighting that achieves compromise between sensitivity and resolution (AIPS ROBUST −1). Additionally, with a well-sampled *uv*-plane that has good coverage on short baselines, at 325 MHz the GMRT is sensitive to structures up to around 32 arcmin in extent. Given that no mJy or sub-mJy sources are expected to exhibit angular sizes on these scales, we would expect no limitation on the size of source that can be recovered due to our *uv*-coverage.

The other aspect of this first effect is that sources with sufficiently high integrated flux density to contribute to the source counts may be resolved to the extent that the peak falls below the detection limit of the source detection algorithm. In order to correct for this effect, we compare the maximum recoverable angular scale with the underlying size distribution to estimate the fraction of sources missed as a function of flux density. For a source of a given flux density, there exists a maximum angular size that can still be recovered by our catalogue. This is given by

$$[\Theta_{\max}(S)]^2 = \left\{ \int_0^{S/A_S} \sqrt{\frac{S B_{\mathrm{maj}} B_{\mathrm{min}}}{A_S z}} f_{\tilde{\sigma}}(z)\, dz \right.$$
$$\left. \times \left[\int_0^{S/A_S} f_{\tilde{\sigma}}(z')\, dz' \right]^{-1} \right\}^2 - B_{\mathrm{maj}} B_{\mathrm{min}}, \quad (6)$$

where $\Theta_{\max}(S)$ is the maximum deconvolved angular size at flux density S, A_S is the signal-to-noise ratio threshold (in this work, 5.0) and B_{maj} and B_{min} are the major and minor axes of the restoring beam, respectively. The *effective* noise at a given position, $\tilde{\sigma}(x, y)$ is defined as the local rms noise divided by the local bandwidth smearing ratio, i.e. $\tilde{\sigma}(x, y) = \sigma(x, y)/\overline{\omega}(x, y)$. By definition, $f_{\tilde{\sigma}}$ is a probability distribution function for $\tilde{\sigma}$; in practice this takes the form of a normalized histogram of $\tilde{\sigma}$ values.

In their work, H14 present the formalism for deriving the bandwidth smearing correction in the case of a non-circular restoring beam. For a source at a given position angle, ζ (in degrees east of north) with respect to the phase centre of observations, the projected beam is given by

$$B_{\mathrm{proj}}(\zeta) = \frac{B_{\mathrm{maj}} B_{\mathrm{min}}}{\sqrt{\left[B_{\mathrm{maj}} \sin(\zeta - \psi)\right]^2 + \left[B_{\mathrm{min}} \sin(\zeta - \psi)\right]^2}}, \quad (7)$$

where ψ is the position angle of the restoring beam (H14). In this work, our mosaic was created using a common circular restoring beam of FWHM 13 arcsec, hence $B_{\mathrm{maj}} = B_{\mathrm{min}} = 13$ arcsec, and $\psi = 0$. Equation (7) was used to derive the effect of bandwidth smearing using the formalism from H14 via

$$\overline{\omega}(x, y) = \frac{S_{\mathrm{peak}}}{S_{\mathrm{peak}}^0} = \left\{ 1 + \frac{2 \ln 2}{3} \left[\frac{\delta \nu_{\mathrm{eff}}}{\nu_{\mathrm{ref}}} \frac{d}{B_{\mathrm{proj}}} \right] \right\}^{-1/2}, \quad (8)$$

where S_{peak} and S_{peak}^0 are the measured and true peak flux densities, respectively, and d is the distance from the pointing centre. In this work, the effective channel width $\delta \nu_{\mathrm{eff}} = 520.8$ kHz. Additionally, the reference frequency at which calibration solutions were derived $\nu_{\mathrm{ref}} = 322.9$ MHz. Equation (8) was evaluated for each pixel of the

individual pointing images, and subsequently mosaicked using the same procedure and weighting as for the field images. The resulting bandwidth smearing mosaic yields $S_{\text{peak}} / S_{\text{peak}}^0 > 0.96$ everywhere, with a typical smearing of less than 2 per cent.

H14 model the true size distribution for total intensity *components* using a modified version of the integral angular size distribution presented by Windhorst, Mathis & Neuschaefer (1990) for *sources* at 1.4 GHz. From Windhorst et al. (1990) the fraction of sources with a largest angular size (LAS) larger than Θ is given by

$$h(> \Theta, S) = 2^{-(\Theta/\Theta_{\text{median}})^{0.62}}, \tag{9}$$

where Θ_{median} is the median LAS as a function of flux density. For single component sources, H14 find their data are better fit by a model that predicts a median LAS that is half the size predicted by Windhorst et al. (1990). H14 give the density function associated with equation (9) as

$$f_\Theta(\Theta, S) = \frac{0.62 \ln 2}{\Theta_{\text{med}}} \left(\frac{\Theta}{\Theta_{\text{med}}} \right)^{-0.38} h(> \Theta, S). \tag{10}$$

The angular size distribution for sources at 325 MHz is less well explored in the literature than at higher frequency, particularly at increasingly faint flux densities. Owen et al. (2009) report higher resolution data (6.37 × 5.90 arcsec) at the same frequency considered in this work; they find a median size distribution consistent with the 1.4 GHz work by Windhorst (2003) scaled to 325 MHz. Recent work with LOFAR by Williams et al. (2016) also evaluated the effect of resolution bias using the Windhorst (2003) distribution scaled to 150 MHz.

With a resolution of 13 arcsec, our observations are unable to probe the angular size distribution of faint sources further than Owen et al. (2009). The resolution of our survey is far more comparable to the resolution of H14. For this derivation we adopt the same formalism for the angular size – flux density relation as H14:

$$\Theta_{\text{median}} = X \text{ arcsec} \left(\frac{S_{1.4 \text{ GHz}}}{1 \text{ mJy}} \right)^{0.30}, \tag{11}$$

where S denotes the source flux density. In their work, H14 use $X = 1$ arcsec, whereas Windhorst (2003) use $X = 2$ arcsec. From theory we would expect that sources become more extended towards lower frequencies, as the lower energy electrons have longer radiative lifetimes, and may travel further from their place of origin. As such, we tested two versions of this distribution, using $X = 1$ (2) arcsec as per H14 (Windhorst 2003) with flux densities scaled to 325 MHz using a spectral index $\alpha = -0.8$, following Williams et al. (2016). We find that using $X = 2$ arcsec provided a correction effect that brought our counts more in line with what is predicted by models and expected from other observations with similar sensitivity.

From H14 therefore, the overall correction for incompleteness due to highly extended sources is given by

$$\frac{\text{d}N_{\text{detectable}}}{\text{d}S} = \frac{\text{d}N_{\text{true}}}{\text{d}S} \times \{1 - h(> \Theta_{\text{max}}(S), S)\}, \tag{12}$$

where $\text{d}N_{\text{true}}/\text{d}S$ is the *true* source counts distribution, and $\text{d}N_{\text{detectable}}/\text{d}S$ is the observable source counts (i.e. sources with angular size $\Theta \leq \Theta_{\text{max}}$). Consequently, the overall correction factor for this first effect, $r_{\text{effect 1}}$, is given by

$$r_{\text{effect 1}}(S) = \frac{\text{d}N_{\text{detectable}}}{\text{d}S}(S) \div \frac{\text{d}N_{\text{true}}}{\text{d}S}(S). \tag{13}$$

6.3.2 Effect 2: underestimation of flux density for unresolved sources

The second form of resolution bias arises as a result of underestimation of the flux density of sources classified as unresolved. From simulations, Bondi et al. (2008) found that a significant fraction of sources with flux densities below 150 μJy were redistributed to *lower* flux densities as a result of poor signal-to-noise prohibiting full deconvolution. H14 derive the formalism for correcting for this effect.

In this work, we have used a different function (equation 3) than that of H14 to describe the locus used to differentiate between resolved and unresolved sources. For a given flux density S, we find the *minimum* angular size Θ_{min} required for a source to be classified as resolved is given by

$$[\Theta_{\text{min}}(S)]^2 = \left\{ \int_0^{S/A_S} \sqrt{B_{\text{maj}} B_{\text{min}} k^{(S/z)^{-c}}} f_{\tilde{\sigma}}(z) \, \text{d}z \right. $$
$$\left. \times \left[\int_0^{S/A_S} f_{\tilde{\sigma}}(z') \, \text{d}z' \right]^{-1} \right\}^2 - B_{\text{maj}} B_{\text{min}}, \tag{14}$$

where k and c are the fit parameters of the locus that allows us to determine which sources are unresolved (see equation 3 in Section 4.1.5) and the remaining parameters are defined as for equation (6). The differential number counts for detectable resolved sources are given by

$$\frac{\text{d}N_{\text{resolved}}}{\text{d}S}(S) = \frac{\text{d}N_{\text{detectable}}}{\text{d}S}(S)$$
$$\times [\, h(> \{\min(\Theta_{\text{min}}(S), \Theta_{\text{max}}(S))\}, S)$$
$$- h(> \Theta_{\text{max}}(S), S)\,]$$
$$\div [\, 1 - h(> \Theta_{\text{max}}(S), S)\,]. \tag{15}$$

Assuming the flux density recovered for resolved sources is equal to their true flux density, we can predict the differential source counts for detectable, unresolved components via

$$\frac{\text{d}N_{\text{unresolved}}}{\text{d}S}(S) = \frac{\text{d}N_{\text{detectable}}}{\text{d}S}(S) - \frac{\text{d}N_{\text{resolved}}}{\text{d}S}(S). \tag{16}$$

In the absence of any measurement error, for an unresolved source the integrated flux density is equal to the integrated surface brightness recovered by our instrument. However, from Fig. 8 it can be seen that some sources have been recovered which appear to have an integrated flux density S_{int} less than the peak flux density S_{peak}. These sources have clearly been affected by noise, and we have assumed $S_{\text{int}} = S_{\text{peak}}$. However, this is based on the assumption of zero intrinsic angular size, whereas sources always have non-zero physical size. As such, sources are pushed towards fainter flux density bins (H14). This effect can be modelled using the formalism of H14 via

$$\frac{\text{d}N_{\text{unresolved,observed}}}{\text{d}S}(S) = \int_S^\infty \frac{\text{d}N_{\text{unresolved}}}{\text{d}S'}(S') \, H\left(\tilde{\Theta} - \Theta' \right)$$
$$\times \frac{f_{\Theta'}(\Theta', S')}{\int_0^{\tilde{\Theta}} f_\Theta(\Theta'', S') \, \text{d}\Theta''} \text{d}S' \tag{17}$$

where $H(x)$ is a step function, given by

$$H(x) = \begin{cases} 1 : & x \geq 0 \\ 0 : & x < 0 \end{cases} \tag{18}$$
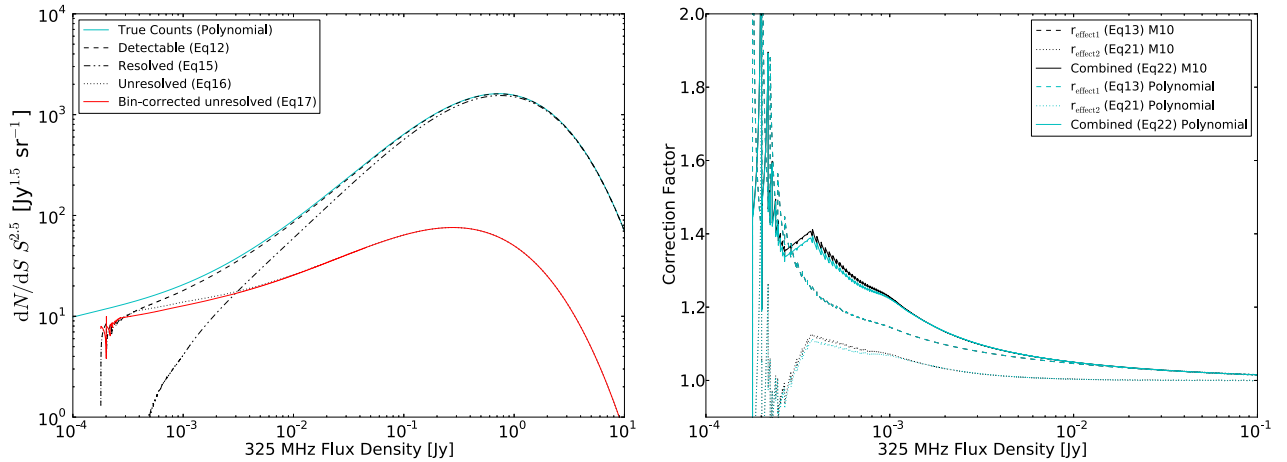
Figure 15. Left-hand panel: the effect of resolution bias on differential source counts, showing the following results: true source counts model from the polynomial model (cyan), detectable source counts (equation 12, dashed), resolved sources (equation 15, dot–dashed), unresolved sources assuming no systematics (equation 16, dotted) and unresolved sources corrected for flux density underestimation (equation 17, red). Right-hand panel: resolution bias correction factors, to account for incompleteness due to highly extended sources (equation 13, dashed line), flux density underestimation for resolved sources (equation 21, dotted line) and the overall combined correction factor (equation 22, solid line). Black (cyan) curves denote the corrections derived assuming the M10 (polynomial fit) model.

and Θ' and $\tilde{\Theta}$ are defined by

$$\Theta' = \sqrt{B_{\mathrm{maj}}\, B_{\mathrm{min}} \left(\frac{S'}{S} - 1\right)} \qquad (19)$$

and

$$\tilde{\Theta} = \min[\Theta_{\mathrm{min}}, \Theta_{\mathrm{max}}]. \qquad (20)$$

To derive the overall correction factor for this second effect, we first derive the minimum angular size using equation (14) for test flux densities across the entire range covered by our survey. Subsequently we use this minimum size as well as the maximum size given by equation 6 to evaluate equations (15) and (17), and use these to derive the correction for this second effect via

$$r_{\mathrm{effect}\,2}(S) = \frac{\mathrm{d}N_{\mathrm{detectable}}}{\mathrm{d}S}(S)$$
$$\div \left[\frac{\mathrm{d}N_{\mathrm{resolved}}}{\mathrm{d}S}(S) + \frac{\mathrm{d}N_{\mathrm{unresolved,observed}}}{\mathrm{d}S}(S)\right]. \qquad (21)$$

6.3.3 Overall resolution bias correction

Following H14 therefore the overall correction factor which accounts for both forms of resolution bias, $R(S)$ is given by

$$R(S) = r_{\mathrm{effect}\,1}(S) \times r_{\mathrm{effect}\,2}(S). \qquad (22)$$

Many previous low-frequency radio surveys have not achieved the depth where the effect of resolution bias becomes significant, or have typically only applied corrections for image area detection fraction.

6.3.4 Evaluating the resolution bias correction

(Massardi et al. 2010, hereafter M10) present a comprehensive evaluation of the various source populations recovered by radio surveys across a wide range of frequencies. The M10 model includes the contribution from AGN-type sources (BL-Lac objects, FSRQ and steep-spectrum objects) as well as SFG and starburst galaxies (SBG). The 325 MHz model suggests a source counts distribution

that flattens below 1 mJy, as has been detected in many previous surveys. However, the raw counts from our work (presented later) suggest a source counts distribution that drops off significantly at the faintest flux densities. In order to investigate the effect of resolution bias, we derive the corrections assuming two models. First, we derive the corrections assuming the model of M10. Following Hopkins et al. (2003), we also derive a fourth-order polynomial fit of the form

$$\log\left[(\mathrm{d}N/\mathrm{d}S)\, S^{2.5}\right] = \sum_{i=0}^{4} a_i \left[\log(S)\right]^i, \qquad (23)$$

where S is the flux density, measured in Jy. In order that our corrections converge to a stable result, we iterated through the polynomial fitting/bias correction derivation process three times. The coefficients of the final fit are as follows: $a_0 = 3.192 \pm 0.172$, $a_1 = -0.223 \pm 0.428$, $a_2 = -0.846 \pm 0.361$, $a_3 = -0.261 \pm 0.120$, $a_4 = -0.024 \pm 0.013$. This fit is valid for flux densities between 242 μJy and 0.74 Jy; additional data at higher flux densities would be required to improve the fit in bright source regime.

The equations presented in this section were evaluated with the chosen model in place of $\mathrm{d}N_{\mathrm{true}}/\mathrm{d}S$. The modelled effects of resolution bias on the differential source counts (assuming the polynomial fit describes the underlying counts distribution) are presented in the left-hand panel of Fig. 15, and the overall correction factor for resolution bias (for both the polynomial model and the M10 model) in the right-hand panel of Fig. 15.

From Fig. 15, it appears that incompleteness due to sensitivity to resolved sources is in excess of the 5 per cent level at around 10 mJy, and becomes more significant below around 1 mJy. It also appears that the redistribution of sources to different flux density bins is most significant for flux densities between a few mJy and a few hundred μJy. This is exemplified by the correction factor in the right-hand panel of Fig. 15, where the overall correction factor rises with decreasing flux density, before falling, and then subsequently rising again as incompleteness dominates at the very faintest flux densities.

The resolution bias correction profile exhibited in Fig. 15 is similar to that derived by H14, including the oscillations towards the
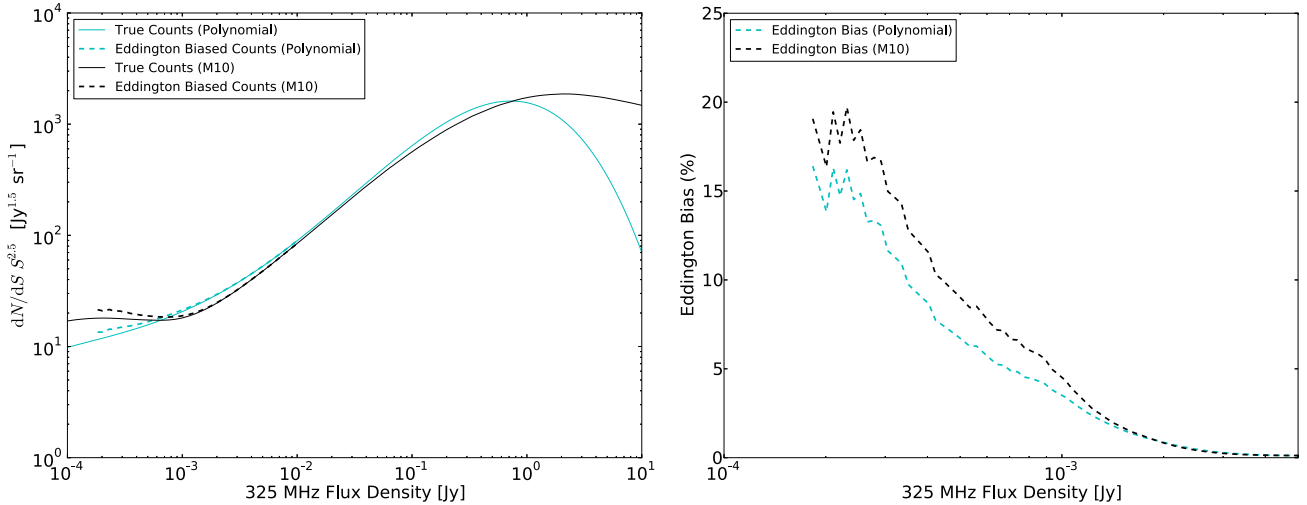
Figure 16. Left-hand panel: the effect of Eddington bias on differential source counts. The cyan (black) curves indicate the source counts for the polynomial fit (M10) model. Dashed curves indicate the modelled effect of Eddington bias, solid curves indicate the underlying distribution. Right-hand panel: the percentage effect of Eddington bias on the source counts model for the region below 5 mJy, where Eddington bias becomes significant. Cyan (black) curves again indicate the polynomial (M10) model described by equation (23).

very faintest flux densities. These are due to the sensitivity across the field, exhibited in Fig. 2, which appears to vary more significantly than the sensitivity in H14. However, our results should not be affected by the large oscillations towards very faint flux densities in Fig. 15 as our faintest bin has a typical flux density of 242 μJy, a regime where the gradient across the bin should not be too significant. Resolution bias corrections were applied per bin when the effect was at the 2 per cent level or higher.

6.4 Eddington bias

As source number counts drop off rapidly with increasing flux density, it is more likely that noise will scatter fainter sources to higher flux densities rather than vice versa. This is known as Eddington bias, and we naturally expect this effect to be most significant at the faint flux density limit of our survey, where number counts are higher. In general, previous work at higher frequency has quantified Eddington bias using semi-empirical methods. For example, Moss et al. (2007) use a source counts model fitted to their data to generate a population of sources below the detection limit. Subsequently, Moss et al. (2007) derive counts from this population and use the difference between the recovered population and input model to quantify the Eddington bias.

H14 also present a robust formalism for deriving the correction due to Eddington bias. We computed the effect of Eddington bias using the formalism of H14 by assuming the differential source counts model from M10, including contributions from AGN, SFG and SBG. As with the resolution bias, we also derived the corrections using our sixth-order polynomial fit, iterating through the fit/correction process three times. From H14, the proportion of components with a *true* flux density $S + \varepsilon$ that are observed to have a flux density S resulting from a Gaussian measurement error $-\varepsilon$ is given by

$$
\frac{\mathrm{d}N_{\mathrm{Edd}}}{\mathrm{d}S}(S) = \int_{-\infty}^{\infty} \int_{0}^{z''} \frac{1}{\sqrt{2\pi}} \exp\left(\frac{-\xi^2}{2}\right)
$$
$$
\times \frac{\mathrm{d}N_{\mathrm{True}}}{\mathrm{d}S}(S + \xi z) \frac{f_{\bar{\sigma}}(z)}{\int_{0}^{z''} f_{\bar{\sigma}}(z')\,\mathrm{d}z'}\,\mathrm{d}z\,\mathrm{d}\xi, \qquad (24)
$$

where $\mathrm{d}N_{\mathrm{Edd}}/\mathrm{d}S$ denotes the biased source counts. The limit of the integral over z is given by

$$
z'' = \begin{cases} S/A_S & : \xi \geq 0 \\ \min\left(-S + \xi,\ S/A_S\right) & : \xi < 0. \end{cases} \qquad (25)
$$

In equation (24) and (25), A_S and $f_{\bar{\sigma}}(z)$ are defined as for equation (6). Note that equation (25) differs from the equivalent equation in H14 (equation 44). This modification was necessary to account for the variable sensitivity across the FOV, ensuring that for a given flux density bin we do not integrate over regions where the noise level would prevent sources being detected.

Eddington bias corrections were derived only for flux densities below a few mJy, as these flux densities begin to approach the noise level in our survey. This correction relies on the assumption that the sources are unresolved. For the flux density range where Eddington bias is likely to be most significant, this is an appropriate assumption – see Section 4.1.5.

Fig. 16 presents the effect of Eddington bias on the assumed underlying source counts, as well as the absolute value of the Eddington bias. In Fig. 16, the cyan (black) curves denote the polynomial fit described by equation (23) (M10 model). From Fig. 16, Eddington bias exceeds the 5 per cent level for flux densities below around 1 mJy. However, from Fig. 16 there is slight discrepancy in the predicted effect of Eddington bias: for all flux density bins below 1 mJy, the M10 model predicts an excess Eddington bias at around the 2 per cent level.

The difference between the two curves in the right-hand panel of Fig. 16 arises naturally as a result of the gradient of the source counts distribution. The M10 models suggest that the Euclidean-normalized source counts are approximately flat from 1 mJy to below the flux density limit of this survey; as such the non-Euclidean differential source counts continue to rise, so the likelihood of sources being upscattered by noise is greater, and Eddington bias rises. Equation (23) predicts a slightly less significant flattening in the Euclidean-normalized counts, meaning the gradient of the non-Euclidean source counts is shallower, and the effect of Eddington bias is reduced. Eddington bias corrections were
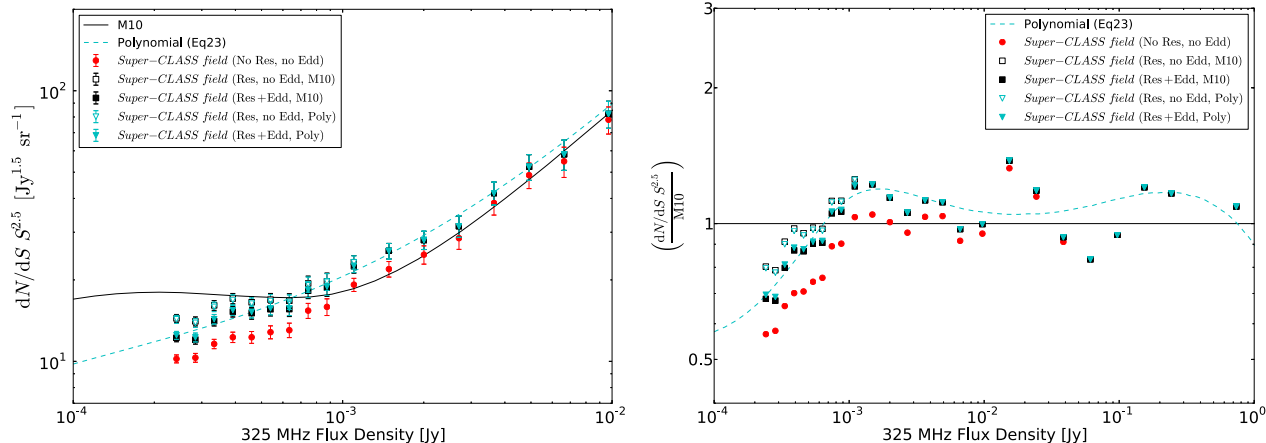
Figure 17. Euclidean-normalized differential source counts at 325 MHz derived from the SCG325 catalogue, showing the effect of the corrections for resolution and Eddington bias below 10 mJy. Black squares (purple triangles) indicate the effect of bias corrections derived assuming the M10 (polynomial, equation 23) model. Filled (open) symbols mark the differential source counts corrected for resolution and Eddington (only Eddington) bias. Filled red points mark the Euclidean-normalized differential source counts prior to resolution and Eddington bias correction. Left-hand panel presents a zoom on the region below 10 mJy, right-hand panel presents the residual compared to the M10 model.

subsequently applied per-bin when the effect was at the 2 per cent level or greater.

6.5 A note regarding model selection

Throughout this section, we have derived the corrections for resolution and Eddington bias for two cases – the polynomial fit to our data as well as the SH12 model. Fig. 17 presents the Euclidean-normalized differential source counts derived from the SCG325 catalogue, with corrections for resolution bias and Eddington bias, assuming both models, as well as the residual between our differential source counts and the M10 model.

From Fig. 17, it appears that the choice of model has a relatively small effect on the overall differential source counts. For the faintest flux density bin, the corrections derived from the polynomial fit model yield differential source counts that are around 8 per cent higher than those derived assuming the M10 model. This is to be expected given the profiles exhibited in the right-hand panels of Figs 15 and 16, as the resolution bias and Eddington bias corrections have the opposite effects. The difference decreases rapidly with increasing flux density, becoming negligible above around 0.5 mJy. Given that our corrected source counts exhibit a discrepancy with the SH12 model towards the faintest flux densities, we use our polynomial model described by equation (23) to derive the final corrections, which were then applied to the source counts we present here.

6.6 Source counts profile

We present the Euclidean-normalized differential source counts in Fig. 18, with the numerical models from M10 for AGN, SFG and SBG, shown, respectively, by the dashed, dotted and dot–dashed curves. The sum of contributions from AGN, SFG and SBG is denoted by the solid black curve. The polynomial described by equation (23) is denoted by the dashed cyan curve. Also shown in Fig. 18 are the Euclidean-normalized source counts derived in previous works with the GMRT (Sirothia et al. 2009; Mauch et al. 2013) as well as the 324 MHz VLA-COSMOS survey (Smolčić et al. 2014) and the SWIRE field (Owen et al. 2009).

From Fig. 18, our source counts profile is consistent with models that suggest that steep-spectrum objects dominate above a few mJy. The contribution from SFG becomes increasingly important at flux densities below a few mJy. The functional form of the normalized source counts derived in this work closely follows the models derived by M10. This is exemplified in the lower panel of Fig. 18, where we present the ratio of the observed source counts to the M10 model; for all bins above 0.33 mJy, the fractional difference is typically less than 20 per cent.

It can be seen in Fig. 18 that we detect the same flattening in the Euclidean-normalized source counts distribution that has been seen in previous surveys at higher frequencies (for example, Garn et al. 2008b, and references therein) and deep GMRT surveys at 325 MHz (Owen et al. 2009; Sirothia et al. 2009, 2010). Additionally, the observations presented in this work are among the first low-frequency studies with sufficient sensitivity to probe the source counts distribution at flux densities where a secondary drop has been seen at higher frequency (1.4 GHz flux density less than around 100−150 μJy; Bondi et al. 2008).

However, some works at 1.4 GHz have not seen this feature (for example, Owen & Morrison 2008) and this has not yet been reported at 325 MHz or 610 MHz. Given a typical synchrotron spectral index of $\alpha = -0.7$, this secondary drop would appear at a 325 MHz flux density of around 280−416 μJy, well within the range of flux densities recovered in this work (our source counts are derived down to a limiting flux density of 242 μJy).

From Fig. 18 there is marginal evidence of this feature at faint flux densities ($S < 308$ μJy), as our source counts profile drops significantly below the predictions of M10. However, given that the resolution bias correction is heavily influenced by the assumed underlying source size distribution model, we cannot discount the possibility that this may be due to a differences between the *true* size distribution of low-frequency radio sources and the model we have assumed.

7 CONCLUSIONS

We report deep 325 MHz GMRT observations of the Super-CLASS field, a region of sky known to contain 5 Abell clusters. We achieve a nominal sensitivity of 34 μJy beam^{-1} towards the centre of the
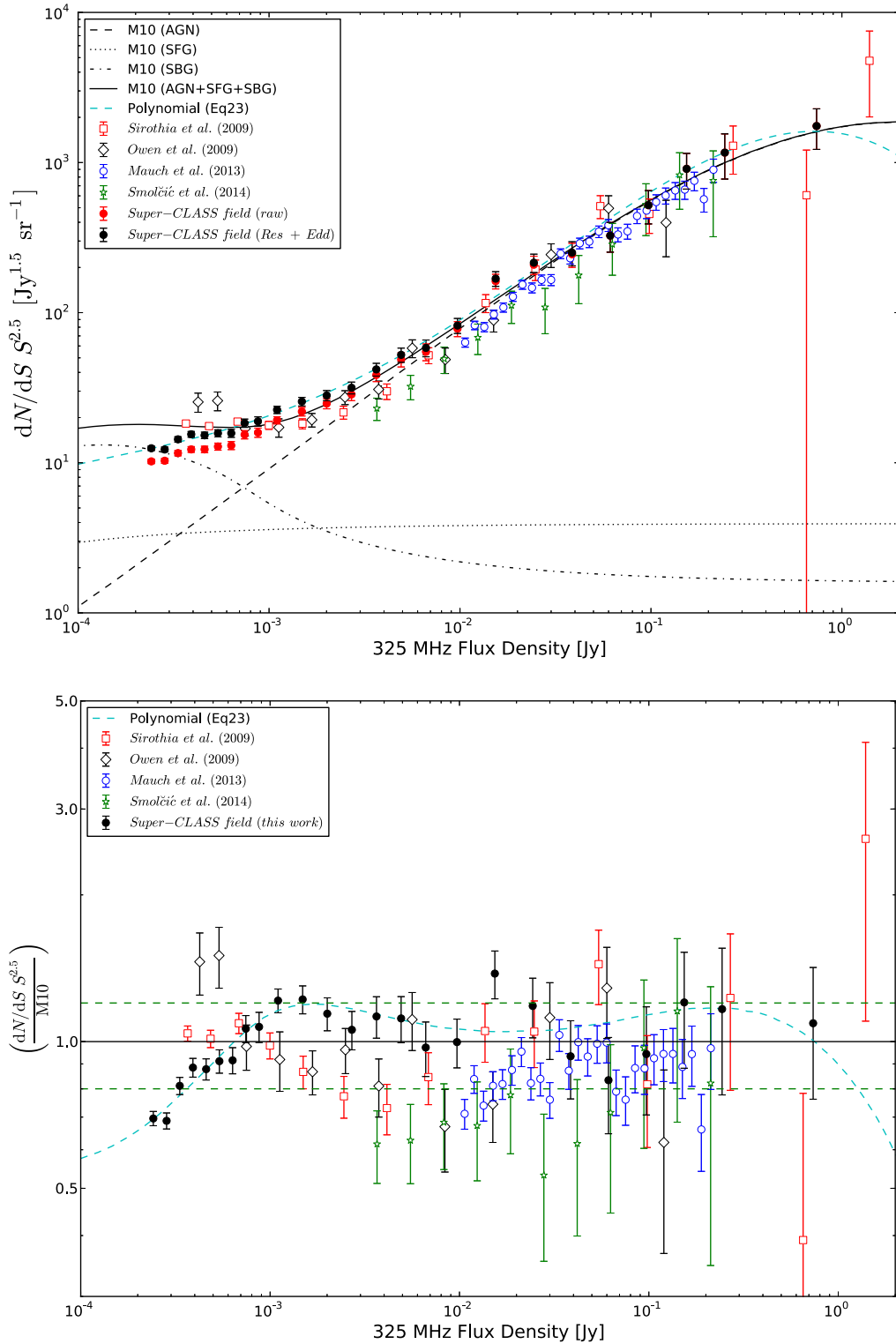
Figure 18. Top panel: Euclidean-normalized differential source counts at 325 MHz for sources detected in this work, corrected for resolution bias and Eddington bias (filled black circles). Note that filled red circles show the source counts from this field prior to resolution and Eddington bias correction, for comparison. We also show the Euclidean-normalized differential source counts from Sirothia et al. (2009) for the ELAIS-N1 field, those of Mauch et al. (2013) for the *Herschel*-ATLAS/GAMA field, those derived by Smolčić et al. (2014) for the VLA-COSMOS field, and those from Owen et al. (2009) for the SWIRE field. Dashed/dot–dashed/dotted curves denote the expected contribution at 325 MHz from AGN/starburst galaxies (SBG)/spiral galaxies (SFG), respectively, from the model of M10; the solid line represents the sum of the populations. The dashed cyan curve denotes the fourth-order polynomial fit to the source counts derived in this work, from equation (23). Bottom panel: observed counts from the literature relative to the total M10 model (AGN+SBG+SFG) illustrating the large scatter in source counts. Dashed cyan curve is the fourth-order polynomial fit relative to the M10 model. Dashed green lines indicate the limit of ±20 per cent compared to the M10 model.

field, the deepest study conducted at this frequency to-date. From our mosaicked image, which covers approximately 6.5 deg^2, we recover a catalogue of 3257 sources down to a flux density limit of 183 µJy.

We have compared with available catalogues from other surveys, and identified 335 sources in common with the NVSS, after accounting for sources which become resolved in the higher resolution GMRT data. The spectral index distribution indicates two populations within the data: a more numerous population of sources centred around a spectral index of $\alpha = -0.81$, which dominate at higher flux densities, and a less numerous, fainter population of sources with flat and rising spectra, which appear to dominate the fainter flux densities. However, this spectral index sample is currently severely limited by the sensitivity of the high-frequency reference.

Adopting the definition of a USS object as a radio source with $\alpha < -1.3$ (as is typically the case in the literature) we find a total of four USS radio sources which have counterparts in the NVSS. Of these, we identify two AGN-type sources whose steep spectra may be the result of our superior sensitivity to faint diffuse emission, and two candidate HzRGs.

Additionally, we have identified three GPS sources, and a further candidate GPS source which is not identified elsewhere in the literature aside from the NVSS. One of these GPS sources is the blazar candidate CGRaBS J1015+6728; we recover an integrated flux density of 3.09 ± 0.31 mJy, to our knowledge the first flux density measurement for this object below 1 GHz. We model the spectra of these GPS sources using a broken power-law; our fits suggest break frequencies in the 2–3 GHz range.

Finally, we derive the Euclidean-normalized differential source counts for sources with flux densities in excess of 223 µJy. We have performed a rigorous mathematical treatment of the various biases in the differential source counts, including Eddington bias and resolution bias. The differential source counts appear to be consistent with predictions from numerical models which account for steep-spectrum sources (AGN, FSRQ and BL Lac objects) and SFG (spiral galaxies and SBG). We have also provided a new empirical model for describing the Euclidean-normalized differential source counts that is valid between 242 µJy and 0.74 Jy.

The source counts distribution derived in this work exhibits marginal evidence of a secondary downturn at flux densities below 308 µJy. This corresponds well with the flux density regime where this feature has been detected at 1.4 GHz. To our knowledge, this is the first detection of this feature in the differential source counts at 325 MHz.

REFERENCES

Abell G. O., Corwin H. G., Jr, Olowin R. P., 1989, ApJS, 70, 1
Afonso J., Georgakakis A., Almeida C., Hopkins A. M., Cram L. E., Mobasher B., Sullivan M., 2005, ApJ, 624, 135
Baars J. W. M., Genzel R., Pauliny-Toth I. I. K., Witzel A., 1977, A&A, 61, 99
Becker R. H., White R. L., Edwards A. L., 1991, ApJS, 75, 1
Becker R. H., White R. L., Helfand D. J., 1994, in Crabtree D. R., Hanisch R. J., Barnes J., eds, ASP Conf. Ser. Vol. 61, Astronomical Data Analysis Software and Systems III. Astron. Soc. Pac., San Francisco, p. 165
Bonaldi A., Harrison I., Camera S., Brown M. L., 2016, preprint (arXiv:1601.03948)
Bondi M., Ciliegi P., Schinnerer E., Smolčić V., Jahnke K., Carilli C., Zamorani G., 2008, ApJ, 681, 1129
Bonzini M., Padovani P., Mainieri V., Kellermann K. I., Miller N., Rosati P., Tozzi P., Vattakunnel S., 2013, MNRAS, 436, 3759
Bressan A., Silva L., Granato G. L., 2002, A&A, 392, 377
Brown M. et al., 2015, in Bourke T. L. et al., eds, Proc. Sci., Advancing Astrophysics with the Square Kilometre Array. SISSA, Trieste, 23
Callingham J. R. et al., 2015, ApJ, 809, 168
Casey C. M. et al., 2015, ApJ, 808, L33
Chang T.-C., Refregier A., Helfand D. J., 2004, ApJ, 617, 794
Clemens M. S., Vega O., Bressan A., Granato G. L., Silva L., Panuzzo P., 2008, A&A, 477, 95
Clemens M. S., Scaife A., Vega O., Bressan A., 2010, MNRAS, 405, 887
Cohen A. M., Porcas R. W., Browne I. W. A., Daintree E. J., Walsh D., 1977, Mem. R. Astron. Soc., 84, 1
Cohen A. S., Lane W. M., Cotton W. D., Kassim N. E., Lazio T. J. W., Perley R. A., Condon J. J., Erickson W. C., 2007, AJ, 134, 1245
Condon J. J., 1984, ApJ, 287, 461
Condon J. J., 1992, ARA&A, 30, 575
Condon J. J., Cotton W. D., Greisen E. W., Yin Q. F., Perley R. A., Taylor G. B., Broderick J. J., 1998, AJ, 115, 1693
Condon J. J., Cotton W. D., Greisen E. W., Yin Q. F., Perley R. A., Taylor G. B., Broderick J. J., 2002, VizieR Online Data Catalog, 8065, 0
De Breuck C., Downes D., Neri R., van Breugel W., Reuland M., Omont A., Ivison R., 2005, A&A, 430, L1
de Bruyn G. et al., 2000, VizieR Online Data Catalog, 8062, 0
de Zotti G., Massardi M., Negrello M., Wall J., 2010, A&AR, 18, 1
Demetroullas C., Brown M. L., 2016, MNRAS, 456, 3100
Diener C. et al., 2015, ApJ, 802, 31
Douglas J. N., Bash F. N., Bozyan F. A., Torrence G. W., Wolfe C., 1996, AJ, 111, 1945
Fomalont E. B., Kellermann K. I., Cowie L. L., Capak P., Barger A. J., Partridge R. B., Windhorst R. A., Richards E. A., 2006, ApJS, 167, 103
Garn T., Green D. A., Riley J. M., Alexander P., 2008a, MNRAS, 383, 75
Garn T., Green D. A., Riley J. M., Alexander P., 2008b, MNRAS, 387, 1037
Gower J. F. R., Scott P. F., Wills D., 1967, Mem. R. Astron. Soc., 71, 49
Gregory P. C., Condon J. J., 1991, ApJS, 75, 1011
Gregory P. C., Scott W. K., Douglas K., Condon J. J., 1996, ApJS, 103, 427
Gruppioni C. et al., 1999, MNRAS, 305, 297
Hales S. E. G., Masson C. R., Warner P. J., Baldwin J. E., 1990, MNRAS, 246, 256
Hales S. E. G., Waldram E. M., Rees N., Warner P. J., 1995, MNRAS, 274, 447
Hales S. E. G., Riley J. M., Waldram E. M., Warner P. J., Baldwin J. E., 2007, MNRAS, 382, 1639

Hales C. A., Norris R. P., Gaensler B. M., Middelberg E., 2014a, MNRAS, 440, 3113

Hales C. A. et al., 2014b, MNRAS, 441, 2555 (H14)

Harrison I., Camera S., Zuntz J., Brown M. L., 2016, preprint (arXiv:1601.03947)

Haslam C. G. T., Klein U., Salter C. J., Stoffel H., Wilson W. E., Cleary M. N., Cooke D. J., Thomasson P., 1981, A&A, 100, 209

Healey S. E., Romani R. W., Taylor G. B., Sadler E. M., Ricci R., Murphy T., Ulvestad J. S., Winn J. N., 2007, ApJS, 171, 61

Healey S. E. et al., 2008, ApJS, 175, 97

Heywood I., Jarvis M. J., Condon J. J., 2013, MNRAS, 432, 2625

Hill T. L., Heisler C. A., Sutherland R., Hunstead R. W., 1999, AJ, 117, 111

Hill T. L., Heisler C. A., Norris R. P., Reynolds J. E., Hunstead R. W., 2001, AJ, 121, 128

Hopkins A. M., Afonso J., Chan B., Cram L. E., Georgakakis A., Mobasher B., 2003, AJ, 125, 465

Huchra J. P., Henry J. P., Postman M., Geller M. J., 1990, ApJ, 365, 66

Huynh M. T., Jackson C. A., Norris R. P., Prandoni I., 2005, AJ, 130, 1373

Ibar E., Ivison R. J., Biggs A. D., Lal D. V., Best P. N., Green D. A., 2009, MNRAS, 397, 281

Intema H. T., van der Tol S., Cotton W. D., Cohen A. S., van Bemmel I. M., Röttgering H. J. A., 2009, A&A, 501, 1185

Jackson N., Battye R. A., Browne I. W. A., Joshi S., Muxlow T. W. B., Wilkinson P. N., 2007, MNRAS, 376, 371

Kellermann K. I., Pauliny-Toth I. I. K., Williams P. J. S., 1969, ApJ, 157, 1

Kettenis M., van Langevelde H. J., Reynolds C., Cotton B., 2006, in Gabriel C., Arviset C., Ponz D., Enrique S., eds, ASP Conf. Ser. Vol. 351, Astronomical Data Analysis Software and Systems XV. Astron. Soc. Pac., San Francisco, p. 497

Klamer I. J., Ekers R. D., Hunstead R. W., 2007, in Afonso J., Ferguson H. C., Mobasher B., Norris R., eds, ASP Conf. Ser. Vol. 380, Deepest Astronomical Surveys. Astron. Soc. Pac., San Francisco, p. 213

Kuehr H., Witzel A., Pauliny-Toth I. I. K., Nauber U., 1981, A&AS, 45, 367

Lane W. M., Cotton W. D., van Velzen S., Clarke T. E., Kassim N. E., Helmboldt J. F., Lazio T. J. W., Cohen A. S., 2014, MNRAS, 440, 327

Lovell J. E. J. et al., 2008, ApJ, 689, 108

Lowe S. R., Gawroński M. P., Wilkinson P. N., Kus A. J., Browne I. W. A., Pazderski E., Feiler R., Kettle D., 2007, A&A, 474, 1093

Mainieri V. et al., 2008, ApJS, 179, 95

Marr J. M., Perry T. M., Read J., Taylor G. B., Morris A. O., 2014, ApJ, 780, 178

Massardi M., Bonaldi A., Negrello M., Ricciardi S., Raccanelli A., de Zotti G., 2010, MNRAS, 404, 532 (M10)

Mauch T., Klöckner H.-R., Rawlings S., Jarvis M., Hardcastle M. J., Obreschkow D., Saikia D. J., Thompson M. A., 2013, MNRAS, 435, 650

Mignano A., Prandoni I., Gregorini L., Parma P., de Ruiter H. R., Wieringa M. H., Vettolani G., Ekers R. D., 2008, A&A, 477, 459

Miley G., De Breuck C., 2008, A&AR, 15, 67

Miller N. A. et al., 2013, ApJS, 205, 13

Mitchell K. J., Condon J. J., 1985, AJ, 90, 1957

Mohan N., Rafferty D., 2015, Astrophysics Source Code Library, record ascl:1502.007

Morganti R., Garrett M. A., Chapman S., Baan W., Helou G., Soifer T., 2004, A&A, 424, 371

Moss D., Seymour N., McHardy I. M., Dwelly T., Page M. J., Loaring N. S., 2007, MNRAS, 378, 995

Muxlow T. W. B. et al., 2005, MNRAS, 358, 1159

Myers S. T. et al., 2003, MNRAS, 341, 1

O'Dea C. P., 1998, PASP, 110, 493

O'Dea C. P., Baum S. A., Stanghellini C., 1991, ApJ, 380, 66

Owen F. N., Morrison G. E., 2008, AJ, 136, 1889

Owen F. N., Morrison G. E., Klimek M. D., Greisen E. W., 2009, AJ, 137, 4846

Padovani P., Mainieri V., Tozzi P., Kellermann K. I., Fomalont E. B., Miller N., Rosati P., Shaver P., 2007, in Afonso J., Ferguson H. C., Mobasher B., Norris R., eds, ASP Conf. Ser. Vol. 380, At the Edge of the Universe: Latest Results from the Deepest Astronomical Surveys. Astron. Soc. Pac., San Francisco, p. 205

Padovani P., Mainieri V., Tozzi P., Kellermann K. I., Fomalont E. B., Miller N., Rosati P., Shaver P., 2009, ApJ, 694, 235

Padovani P., Bonzini M., Kellermann K. I., Miller N., Mainieri V., Tozzi P., 2015, MNRAS, 452, 1263

Patel P., Bacon D. J., Beswick R. J., Muxlow T. W. B., Hoyle B., 2010, MNRAS, 401, 2572

Patnaik A. R., Browne I. W. A., Wilkinson P. N., Wrobel J. M., 1992, MNRAS, 254, 655

Pauliny-Toth I. I. K., Witzel A., Preuss E., Kühr H., Kellermann K. I., Fomalont E. B., Davis M. M., 1978, AJ, 83, 451

Prandoni I., Gregorini L., Parma P., de Ruiter H. R., Vettolani G., Wieringa M. H., Ekers R. D., 2000, A&AS, 146, 41

Prandoni I., Gregorini L., Parma P., de Ruiter H. R., Vettolani G., Zanichelli A., Wieringa M. H., Ekers R. D., 2001, A&A, 369, 787

Prandoni I., Parma P., Wieringa M. H., de Ruiter H. R., Gregorini L., Mignano A., Vettolani G., Ekers R. D., 2006, A&A, 457, 517

Randall K. E., Hopkins A. M., Norris R. P., Zinn P.-C., Middelberg E., Mao M. Y., Sharp R. G., 2012, MNRAS, 421, 1644

Remazeilles M., Dickinson C., Banday A. J., Bigot-Sazy M.-A., Ghosh T., 2015, MNRAS, 451, 4311

Rengelink R. B., Tang Y., de Bruyn A. G., Miley G. K., Bremer M. N., Roettgering H. J. A., Bremer M. A. R., 1997, A&AS, 124, 259

Richards E. A., Fomalont E. B., Kellermann K. I., Windhorst R. A., Partridge R. B., Cowie L. L., Barger A. J., 1999, ApJ, 526, L73

Richards J. L. et al., 2011, ApJS, 194, 29

Roger R. S., Costain C. H., Bridle A. H., 1973, AJ, 78, 1030

Rossetti A., Mantovani F., Dallacasa D., Fanti C., Fanti R., 2005, A&A, 434, 449

Roy J., Gupta Y., Pen U.-L., Peterson J. B., Kudale S., Kodilkar J., 2010, Exp. Astron., 28, 25

Sadat R., Blanchard A., Kneib J.-P., Mathez G., Madore B., Mazzarella J. M., 2004, A&A, 424, 1097

Scaife A. M. M., Heald G. H., 2012, MNRAS, 423, L30 (SH12)

Schinnerer E. et al., 2004, AJ, 128, 1974

Schinnerer E. et al., 2010, ApJS, 188, 384

Seymour N. et al., 2007, ApJS, 171, 353

Singh V. et al., 2014, A&A, 569, A52

Sirothia S. K., Dennefeld M., Saikia D. J., Dole H., Ricquebourg F., Roland J., 2009, MNRAS, 395, 269

Sirothia S. K., Saikia D., Burgarella D., 2010, Proc. Science, International SKA Forum 2010. SISSA, Trieste, PoS#51

Smolčić V. et al., 2008, ApJS, 177, 14

Smolčić V. et al., 2014, MNRAS, 443, 2590

Stawarz Ł., Ostorero L., Begelman M. C., Moderski R., Kataoka J., Wagner S., 2008, ApJ, 680, 911

Stevens J. A. et al., 2003, Nature, 425, 264

Tasse C. et al., 2006, A&A, 456, 791

van Haarlem M. P. et al., 2013, A&A, 556, A2

Venemans B. P. et al., 2007, A&A, 461, 823

White R. L., Becker R. H., 1992, ApJS, 79, 331

White R. L., Becker R. H., Helfand D. J., Gregg M. D., 1997, ApJ, 475, 479

Wieringa M. H., 1991, PhD thesis, Rijksuniversiteit Leiden

Williams W. L. et al., 2016, preprint (arXiv:1605.01531)

Windhorst R. A., 2003, New Astron. Rev., 47, 357

Windhorst R. A., Miley G. K., Owen F. N., Kron R. G., Koo D. C., 1985, ApJ, 289, 494

Windhorst R., Mathis D., Neuschaefer L., 1990, in Kron R. G., ed., ASP Conf. Ser. Vol. 10, Evolution of the Universe of Galaxies. Astron. Soc. Pac., San Francisco, p. 389

Witzel A., Pauliny-Toth I. I. K., Geldzahler B. J., Kellermann K. I., 1978, AJ, 83, 475

Wright E. L., 2006, PASP, 118, 1711

Zhang X., Zheng Y., Chen H., Wang S., Cao A., Peng B., Nan R., 1997, A&AS, 121, 59

This paper has been typeset from a TEX/LATEX file prepared by the author.